# Fluidizable La$_2$O$_3$ promoted Ni/γ-Al$_2$O$_3$ catalyst for steam gasification of biomass: Effect of catalyst preparation conditions

Jahirul Mazumder, Hugo I. de Lasa*

*Chemical Reactor Engineering Centre, Department of Chemical and Biochemical Engineering, The University of Western Ontario, London, ON N6A 5B9, Canada*

ABSTRACT

This study reports a new fluidizable La$_2$O$_3$ promoted Ni/γ-Al$_2$O$_3$ catalyst for biomass steam gasification. Catalysts are prepared using a specially designed incipient wetness multi-step impregnation technique with subsequent reduction of metal precursors in a fluidized bed. Catalyst characterization shows that addition of La$_2$O$_3$ up to 5 wt% improves surface area, CO$_2$ adsorption capacity, Ni reducibility and metal dispersion, as well as reduces support acidity. XRD shows undesirable LaAlO$_3$ formation when catalysts with more than 10 wt% La$_2$O$_3$ are calcined above 1000 °C. This result points toward the increase of local catalyst bed temperature during exothermic reduction of metal nitrates. Higher reduction gas flow rates can control the rise of catalyst bed temperature by effectively removing the generated heat. This controlled reduction helps to minimize sintering/dehydroxylation of the metastable γ-Al$_2$O$_3$, with octahedral and tetrahedral site ratio being used as an indicator of γ-Al$_2$O$_3$ dehydroxylation. The octahedral and tetrahedral site ratios are estimated using H$_2$ TPR and NH$_3$-TPD. Steam gasification experiments are performed in a CREC Riser Simulator under expected conditions of circulating fluidized bed gasifiers using glucose and 2-methoxy-4-methylphenol to represent cellulose and lignin, respectively. Gasification performance of the prepared catalyst is found to be a function of Ni dispersion and support basicity/acidity ratio. It is hypothesized that acid sites of γ-Al$_2$O$_3$ are responsible for coke deposition via hydrocarbon cracking, whereas basic sites facilitate coke reforming. Based on these data, a 20% Ni/5% La$_2$O$_3$-γAl$_2$O$_3$ is developed, in this study, optimizing catalyst formulation and preparation conditions. This catalyst yields a 97% carbon conversion of glucose to permanent gases with no tar formation at 650 °C. In the case of 2-methoxy-4-methylphenol gasification, a 85.5% carbon conversion with only 8.3% tar formation is achieved.

© 2014 Elsevier B.V. All rights reserved.

## 1. Introduction

Biomass gasification is considered as one of the most promising thermochemical processes given its greater energy efficiency and proven operational history [1–7]. Gasification can efficiently and economically convert the low value and highly distributed solid biomass into synthesis gas. Air, oxygen and steam are usually used as gasifying agents. In recent years, biomass steam gasification has become an area of growing interest because it produces a synthesis gas with relatively higher heating value and higher hydrogen content [4,5,8–13]. Steam gasification of biomass in fluidized beds is a promising approach given its: (i) rapid biomass heating, (ii) effective heat and mass transfer between reacting phases, (iii)

uniform gasifier reaction temperature [1,10,13,14]. Moreover, fluidized beds tolerate wide variations in fuel quality as well as broad particle-size distributions.

Steam gasification of biomass involves a complex network of heterogeneous reactions. The gasification process can be classified into three steps: drying, devolatilization and gasification as shown in Fig. 1. One can envision biomass gasification as a combination of primary and secondary reactions [12,14–16]. Primary reactions break down the vaporized biomass molecules, forming permanent gases, higher hydrocarbons, tars and coke. Secondary reactions crack or/and reform the higher hydrocarbons and tars into lighter hydrocarbons and permanent gases. Furthermore, light hydrocarbons, CO and H$_2$ can react with steam and CO$_2$ altering the gas composition depending on gasifier operating conditions.

However, in the implementation of biomass gasification to produce high quality syngas or/and hydrogen, formation of tars still offers a technical challenge [16–19]. Tar formation creates numerous

$$C_nH_{2m} + tars + H_2O \longrightarrow CO + H_2$$

$$CH_4 + H_2O \longleftrightarrow CO + 3H_2 \qquad \Delta H^0 = 205.81 \; kJ/mol$$

$$CH_4 + CO_2 \longleftrightarrow 2CO + 2H_2 \qquad \Delta H^0 = 246.98 \; kJ/mol$$

$$CO + H_2O \longleftrightarrow H_2 + CO_2 \qquad \Delta H^0 = -41.16 \; kJ/mol$$

$$C + H_2O \longleftrightarrow H_2 + CO \qquad \Delta H^0 = 131.29 \; kJ/mol$$

$$C + CO_2 \longleftrightarrow 2CO \qquad \Delta H^0 = 172.46 \; kJ/mol$$

$$C + 2H_2 \longleftrightarrow CH_4 \qquad \Delta H^0 = -74.52 \; kJ/mol$$

$$C_x H_y O_z \xrightarrow{heat} H_2 + CO + CO_2 + H_2O + C_nH_{2m} + C_{(s)} + tars$$
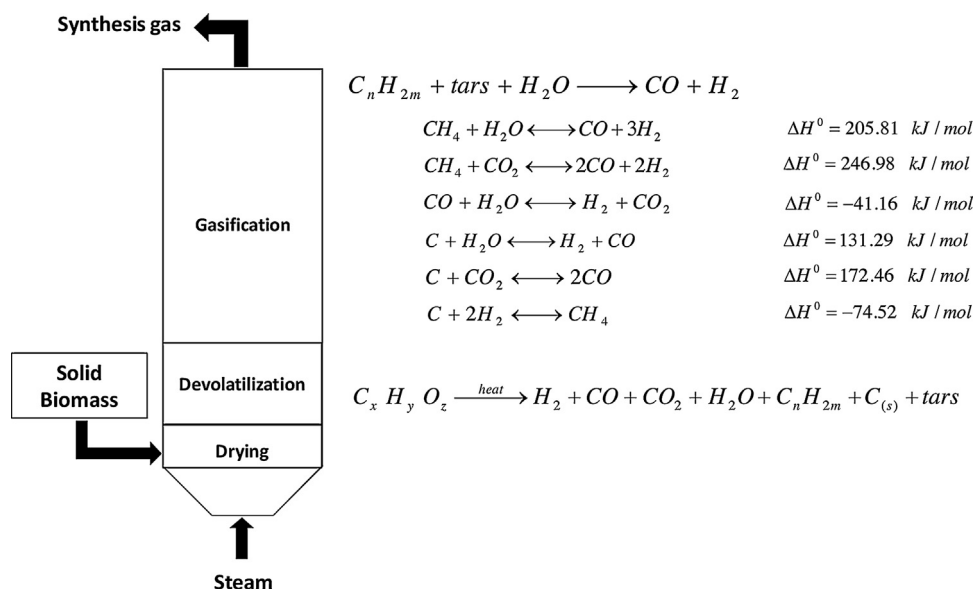
**Fig. 1.** Schematic description of biomass steam gasification process.

problems in gasifier operation, while conversion of tar adds value to the syngas by increasing the yields of $H_2$ and/or CO [20–22]. Tar can be converted thermally. However, this typically requires a very high temperature (greater than 1000 °C) which is not economically viable. Furthermore, this also increases the risk of ash agglomeration. Therefore, the catalytic reforming of biomass tars into gaseous products inside the gasifier appears as an effective and efficient method for tar removal, avoiding costly downstream processing for tar disposal [5,17,22].

An effective catalyst for biomass gasification should be stable and highly active, producing high quality and tar free synthesis gas. Dolomite, olivine, zeolites, alkali and noble metals, as well as nickel-based catalysts have been used for this purpose [5,9,16,22]. The Ni catalyst is one of the most promising catalysts for biomass gasification due to its high reforming activity and affordability [23–27]. Deactivation may be an issue, however, with nickel-based catalysts [22,26–28]. Under the high operating gasification temperatures required to achieve significant feedstock conversion, deactivation of Ni-based catalysts may occur due to coke deposition and crystallite agglomeration. Thus, new catalysts for biomass steam gasification should have the long life required in preventing tar formation, carbon fouling and crystallite agglomeration under the operating conditions of a gasifier [9]. To accomplish this, the use of promoters plays a very important role in minimizing tar formation and in enhancing the stability of Ni-based catalysts [26–29].

Fluidizable $\gamma$-$Al_2O_3$ is one of the most promising supports for a Ni-based catalyst due to its high surface area and mechanical strength. However, $\gamma$-$Al_2O_3$ is not stable at high temperatures due to thermal sintering and phase transformation. In this respect, $La_2O_3$ has been investigated as a $\gamma$-$Al_2O_3$ stabilizer [30–34]. Moreover, $La_2O_3$ has been used as a promoter of Ni/$Al_2O_3$ catalysts for steam gasification of biomass and its surrogate species [26,27,29,35–38]. Regarding $La_2O_3$ addition, it has been proven that controlled $La_2O_3$ amounts disperse well on $\gamma$-$Al_2O_3$. These lanthanum species enhance catalytic activity, acting as a Ni dispersion promoter [34,39–48]. There is, however, a limit for lanthanum loading. Excess lanthanum may lead to the formation of undesirable $LaAlO_3$ above 1000 °C [31,40,41,46,49,50]. Moreover, the controlled amount of basic $La_2O_3$ reduces the acidity and enhances the $CO_2$ adsorption capacity of $\gamma$-$Al_2O_3$ resulting in lower coke formation on the catalyst surface [27,36,43,51–54].

In our previous study [55], it was shown that surface area, dispersion, and reducibility of Ni/$\gamma$-$Al_2O_3$ catalysts could be improved significantly, however, by direct decomposition of nickel salts to nickel in a reducing atmosphere without prior calcinations in air. We also studied the effect of $La_2O_3$ loading on a $\gamma$-$Al_2O_3$ support from Alcan Inc. (Alcan AA-100 Powder) [56]. Moreover, it was shown that a $\gamma$-$Al_2O_3$ sample from Sasol North America Inc. (Sasol Catalox SSCa5/200) has better thermal stability than the Alcan AA-100 support, facilitating Ni dispersion.

The present study focuses on the development of a new Ni/$La_2O_3$-Sasol $\gamma$-$Al_2O_3$ catalyst for the steam gasification of biomass surrogates. The catalyst preparation conditions (reduction gas flow rate) and catalyst formulation are optimized. It is shown that the newly developed catalyst displays encouraging results in terms of conversion of biomass surrogates (glucose and 2-methoxy-4-methyl-phenol), quality of the synthesis gas produced and tar yields. The catalyst structure and reactivity/stability relationship is also established. Moreover, performance of the developed catalyst is also compared with biomass gasification product yields at reaction equilibrium conditions.

## 2. Experimental methods

### 2.1. Catalyst preparation

In this study, Ni-based (Ni/$La_2O_3$/$\gamma$-$Al_2O_3$) catalysts were prepared using a specially designed incipient wetness technique. This involved a multi-step impregnation, with the direct reduction of metal precursors after each impregnation in fluidized bed. $\gamma$-$Al_2O_3$ (Sasol Catalox® SSCa5/200) was used as catalyst support. Ni/$La_2O_3$/$\gamma$-$Al_2O_3$ catalysts were prepared using successive impregnation: (a) $\gamma$-$Al_2O_3$ was modified by adding $La_2O_3$, (b) following this, Ni was added on the modified $\gamma$-$Al_2O_3$ support. $La(NO_3)_3$.$6H_2O$ (CAS 10,277-43-7) and $Ni(NO_3)_2$·$6H_2O$ (CAS 13,478-00-7) received from Sigma–Aldrich were used as precursors for the desired metal loading. The $La_2O_3$ loading was varied from 0 wt% to 15 wt%; whereas, 20 wt% cumulative Ni was loaded in 3 different steps to reduce the nickel–aluminate formation as well as to increase the dispersion.

Three main steps were involved in the catalyst preparation: (a) support impregnation, (b) drying, and (c) metal precursor reduction. After the impregnation of precursor solution, the resulting

paste was dried slowly at 140 °C overnight. The dried powder was then reduced in a specially designed fluidized bed chamber at 700 °C (3 °C/min) for 8 h under the flow of 10% $H_2$–He. It was found that the gas flow rate during catalyst reduction was a key preparation parameter. This was the case, given the gas flow rate determines heat distribution and fluidization conditions inside the catalyst reduction chamber. To study the effect of reduction gas flow, catalysts were prepared by varying the reducing gas flow: (a) Low flow (fixed bed condition): 20% Ni/5% $La_2O_3$-γ-$Al_2O_3$ (_NiLaA-LF_), (b) Medium flow (minimum fluidization): 20% Ni/γ-$Al_2O_3$ (_NiA-MF_) and 20% Ni/5% $La_2O_3$-γ-$Al_2O_3$ (_NiLaA-MF_), and (c) High flow (uniform fluidization): 20% Ni/5% $La_2O_3$-γ-$Al_2O_3$ (_NiLaA-HF_). These catalysts designations are adopted throughout this manuscript.

## 2.2. Catalyst characterization

### 2.2.1. BET analysis
The specific surface area, the average pore radius and pore volume of the prepared catalyst samples were determined in a Micromeritics ASAP 2010 Analyzer by using $N_2$ adsorption at 77 K. For each experiment, 0.1–0.2 g of the catalyst sample was degassed at 573 K for 2.5 h before the analysis. The adsorption isotherms were measured in $10^{-6}$ – 1 relative pressure ranges.

### 2.2.2. Temperature programmed studies
Temperature programmed reduction (TPR), temperature programmed oxidation (TPO), temperature programmed desorption (TPD) and pulse chemisorption experiments were conducted using a Micromeritics Autochem II 2920 Analyzer. Before the hydrogen TPR experiment, the sample was pre-oxidized using a gas containing 5% oxygen in helium at 700 °C. The oxidized sample was then reduced using a gas containing 10% hydrogen in argon at a heating rate of 10 °C/min. The amount of hydrogen consumed ($V_{H_2}$) in the reduction of the catalyst sample was determined from the TCD signal to establish the reducible species in the catalyst sample.

$H_2$ pulse chemisorption was performed at ambient temperature following the TPR experiment. After reduction, a stream of argon gas was flown through the sample bed at a rate of 50 mL/min. Hydrogen gas was then injected as a series of consecutive pulses containing each 1.0 mL using a calibrated loop. The total amount of hydrogen chemically adsorbed on the active sites of the catalyst was used to calculate the percent metal dispersion as follows:

$$\%D = \frac{AX}{Wf} \times 100 \tag{1}$$

where % D is the percentile metal dispersion, A represents a constant parameter [117 g of exposed Ni/mole of $H_2$], X stands for the total hydrogen chemisorbed [mole of $H_2$/gcat], W denotes the metal weight fraction in catalyst [g of Ni/gcat] and f constitutes the fraction of reduced metal [g of reducible Ni/g of Ni].

Furthermore, the average crystal size ($d_v$) of the metal on the support was calculated from the percent metal dispersion using the following equation:

$$d_v = \frac{\varphi V_m}{S_m} \times \frac{1}{\%D} \tag{2}$$

where $V_m$ stands for the volume of metal atoms [nm$^3$/atom], $\varphi$ is the particle shape constant [6 assuming spherical particles] and $S_m$ denotes the average surface area of the metal particles exposed per surface metal atom [nm$^2$/atom].

Ammonia TPD is one of the most widely used techniques to characterize the acid sites on oxide surfaces. Before the TPD experiment, the catalyst sample was pre-treated by flowing He/$H_2$ (in case of Ni loaded samples) at 700 °C. The catalyst sample was then brought to saturation, by flowing a stream of gas containing 5% $NH_3$

in helium at 50 °C for 1 h. After purging for 1 h, the temperature in the bed was raised at a linear rate (15 °C/min) from ambient to 950 °C while a stream of inert He gas was flown throughout the bed. To establish the basicity and $CO_2$ adsorption capacity of the catalyst samples, $CO_2$-TPD was performed using a similar procedure as used for $NH_3$-TPD.

### 2.2.3. X-ray diffraction analysis
X-ray powder diffraction patterns were obtained on a Rigaku Miniflex Diffractometer using Ni filtered Cu Kα (λ = 0.15406 nm) radiation. A tube voltage of 40 kV and a tube current of 20 mA were used with each sample. The samples were scanned every 0.02 degrees from 10 to 100° degrees with a scan time constant of 2 degrees/min. Identification of the phase was made with the help of the Joint Committee on Powder Diffraction Standards (JCPDS) files. The crystallite sizes of Ni were calculated using Scherrer's equation:

$$d = \frac{0.9\lambda}{(\beta - \beta_0)\cos\theta} \tag{3}$$

where d is the volume average diameter of the crystallite and $(\beta - \beta_0)$ is the full width at half maximum of the peak.

### 2.2.4. Pyridine FTIR
Pyridine FTIR was performed to evaluate the nature and strength of acid sites using a Bruker IFS55 FTIR spectrometer. Before pyridine adsorption, the samples were heat treated at 500 °C under $N_2$ flow for 2 h and then cooled to 100 °C. Following this, the samples were saturated using a $N_2$ gas stream containing pyridine for 1 h. In the next step, the catalyst samples were purged with pure $N_2$ at 100 °C for 1 h, to remove weakly adsorbed pyridine. Finally, diffuse reflectance infrared spectroscopy (DRIFTS) measurements were recorded at room temperature using the Bruker IFS55 FTIR spectrometer having a 4 cm$^{-1}$ resolution and data averaging over 100 scans.

## 2.3. CREC Riser Simulator

Steam gasification of glucose (a cellulose surrogate) and 2-methoxy-4-methylphenol (a lignin surrogate) was performed using a CREC Riser Simulator. The CREC Riser Simulator is a bench-scale mini fluidized bed reactor with a volume of 50 cm$^3$. This bench-scale reactor is specially designed for catalyst evaluation under the operating conditions of an industrial circulating fluidized bed reactor. A detailed description of the CREC Riser Simulator can be found elsewhere in the literature [55,57].

The Ni catalysts, already thermally treated during the preparation process, were loaded into the catalyst basket. The reactor system was sealed, leak tested and heated to the reaction temperature in an argon atmosphere. Then, the feed was injected, and once the reaction time was reached, the reaction products were evacuated from the reactor to the vacuum box. Reactor and vacuum box pressure data against time were recorded by the Personal Daq Acquisition Card. After the reaction, the products were quickly evacuated to the vacuum box. From the vacuum box, gas samples were sent to a GCMS system via heated transfer lines. The GCMS system is equipped with a packed-bed column (HaysSep® D) and a capillary column (BPX5). The packed-bed column is connected to a thermal conductivity detector (TCD) and the capillary column is connected to a mass spectrometer (MS).

To remove the deposited coke on the catalyst, catalyst regeneration was performed after every run. Regeneration conditions were 10 min of air flow to combust the coke first, followed by 10 min of hydrogen flow to reduce the catalyst. Coke deposited on the catalyst after the experimental runs was measured as $CO_2$ in a Total Organic

**Table 1**
BET surface area, pore volume and pore diameter of the $La_2O_3$ modified $\gamma$-$Al_2O_3$ samples.

| Sample | $S_{BET}$ (m$^2$/g) | Pore volume (cm$^3$/g) | Avg pore dia (Å) |
|---|---|---|---|
| $\gamma$-$Al_2O_3$ | 193 | 0.51 | 104 |
| $\gamma$-$Al_2O_3$ calcined @ 700 °C | 180 | 0.49 | 109 |
| 2% $La_2O_3$-$\gamma$-$Al_2O_3$ | 182 | 0.50 | 107 |
| 5% $La_2O_3$-$\gamma$-$Al_2O_3$ | 183 | 0.48 | 104 |
| 10% $La_2O_3$-$\gamma$-$Al_2O_3$ | 162 | 0.45 | 107 |
| 15% $La_2O_3$-$\gamma$-$Al_2O_3$ | 144 | 0.42 | 111 |

Carbon Analyzer (TOC-V) using a solid sample module (SSM-5000) from Mandel.

Experiments in the CREC Riser Simulator were repeated at least 4 times to secure reproducibility of the results. Standard deviations for experimental repeats were in the 3–12% range with an average of 6%. An important observation from these runs was that the mass balance closures, which included $H_2$, CO, $CO_2$, $H_2O$, $CH_4$, ethylene, ethane, propylene, acetaldehyde, and carbon deposited over the catalyst, were in the ±11% range, with most of the mass balances closing in the ±5% range.

## 3. Results and discussions

### 3.1. $La_2O_3$ modified $\gamma$-$Al_2O_3$

#### 3.1.1. Textural properties

Table 1 reports BET surface area, pore volume and average pore diameter of the $La_2O_3$ modified $\gamma$-$Al_2O_3$ supports. It can be observed that the incorporation of up to 5 wt% $La_2O_3$ onto $\gamma$-$Al_2O_3$, increases the $S_{BET}$ from 180 to 183 m$^2$/g while compared to the bare calcined $\gamma$-$Al_2O_3$. The average pore diameter of $\gamma$-$Al_2O_3$ is also decreased from 109 to 104 Å. This suggests good dispersion of $La_2O_3$ onto the pores of the $\gamma$-$Al_2O_3$, with $La_2O_3$ coating the inner pore surfaces. However, more than 5 wt% $La_2O_3$ results in a decrease in surface area almost linearly as observed in the case of Alcan $\gamma$-$Al_2O_3$ [56]. Furthermore with 15 wt% $La_2O_3$ loading, the average pore diameter is significantly increased to 111 Å. This can be attributed to the blocking of small pores by an excessive lanthanum addition. Therefore, 5 wt% $La_2O_3$ can be considered as the optimal $La_2O_3$ loading level to preserve the surface structure of $\gamma$-$Al_2O_3$.

#### 3.1.2. Acid–base properties

The type and nature of acidic sites present in $\gamma$-$Al_2O_3$ and in $La_2O_3$ modified $\gamma$-$Al_2O_3$ support were evaluated with DRIFT using pyridine as a probe molecule. Pyridine interacts with different acid sites through the electron lone pair of its nitrogen atoms. Three types of adsorbed pyridine species have been reported as being present [58–60]: (a) Molecularly adsorbed pyridine coordinating its lone electron pair localized in the nitrogen atom with surface Lewis acid sites ($Al^{3+}$), (b) Hydrogen bonded pyridine interacting via its nitrogen atom with weakly acidic hydroxy surface sites, and (c) Pyridinium ion formed by extracting a proton from a Brønsted acid hydroxy surface site. Protonated pyridine on Brønsted centers give bands at 1640 and 1540 cm$^{-1}$, whereas bands in the 1580–1630 cm$^{-1}$ and the 1440–1455 cm$^{-1}$ ranges are characteristic of pyridine coordinated with Lewis acid sites [58–61].

Fig. 2 reports the IR spectra of the $La_2O_3$ doped and bare $\gamma$-alumina supports, following pyridine adsorption and evacuation at 100 °C, in the spectral region of 1700–1400 cm$^{-1}$. No bands at 1540 cm$^{-1}$ for both samples were observed. This indicates that there are no Brønsted acid sites available on the $\gamma$-alumina surface, strong enough to form pyridinium ions. On the other hand, the
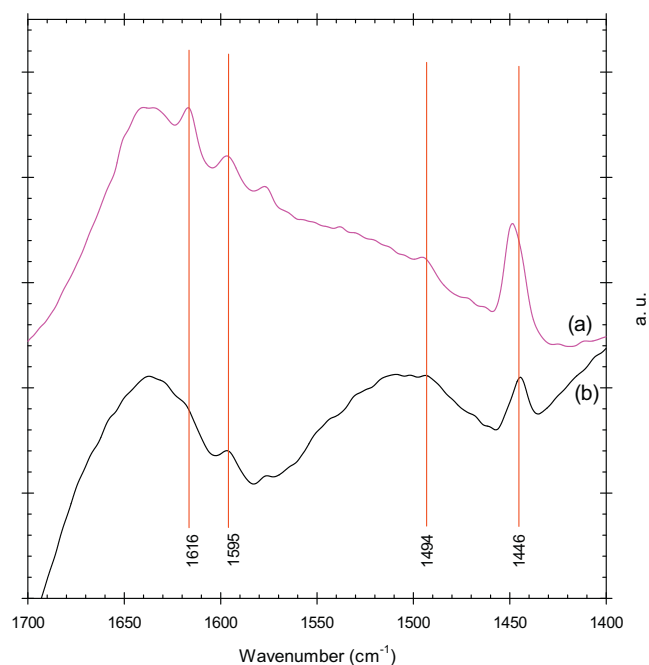


**Fig. 2.** Pyridine DRIFT spectra of (a) $\gamma$-$Al_2O_3$ and (b) 5% $La_2O_3$-$\gamma$-$Al_2O_3$.

appearance of the "19b" band at 1445 cm$^{-1}$ and the "8a" band at 1590–1635 cm$^{-1}$ in the DRIFT spectra of undoped alumina, demonstrates the presence of Lewis acid sites. Based on the multiplicity of the "8a" band of coordinated pyridine, three types of Lewis acid sites with different strengths have been reported in the literature [59,62–64]: weak (1595–1610 cm$^{-1}$), moderate (1610–1620 cm$^{-1}$) and strong (1620–1635 cm$^{-1}$). Assignment of those peaks in terms of $Al^{3+}$ configurations are further discussed in a later section.

$\gamma$-$Al_2O_3$ exhibits peaks at 1595 cm$^{-1}$ and 1616 cm$^{-1}$ in the IR spectra (Fig. 2) indicating the presence of weak to moderate Lewis acid sites. Moreover, the small peak at 1576 cm$^{-1}$ corresponds to the "8b" vibrational mode which is either hydrogen bonded or coordinated pyridine. Furthermore, in the case of the $\gamma$-$Al_2O_3$ modified with 5wt% $La_2O_3$, the intensities of all the 19a,b and 8a bands were significantly decreased.

The acidity and basicity of the supports were further investigated by temperature programmed desorption (TPD) of $NH_3$ and $CO_2$, respectively. Fig. 3 reports $NH_3$-TPD profiles for the undoped and $La_2O_3$ doped $\gamma$-$Al_2O_3$ supports. One can notice that the $\gamma$-$Al_2O_3$ samples yield an asymmetric desorption peak in the low temperature range of 50 to 450 °C. This peak displays a maximum at around 120 °C and a long tail. The low temperature desorption peaks confirm the absence of Brønsted acid sites while the tail can be attributed to the presence of Lewis acid sites with different strengths. A clear bump at around 225 °C, observed in the $NH_3$-TPD profile of $\gamma$-$Al_2O_3$, can be correlated to the pyridine DRIFT peak of moderate strength Lewis acid sites at 1616 cm$^{-1}$ (Fig. 2 and Fig. 3). These peaks almost disappeared from both the TPD profile and the IR spectra with the addition of 5% $La_2O_3$.

$CO_2$-TPD profiles of $La_2O_3$ doped and bare $\gamma$-$Al_2O_3$ samples are reported in Fig. 4. $\gamma$-$Al_2O_3$ samples give a single asymmetric low-temperature (45–300 °C) $CO_2$ desorption peak with a maximum value at 95 °C. According to Morterra et al. [65], this low-temperature desorption peak can be attributed to the low-strength basic sites. These low-strength basicity sites can be traced to bicarbonates, which are formed as a result of the interaction between $CO_2$ and the weak basic surface hydroxyl groups. In addition, the asymmetric $CO_2$ desorption peak shows the coexistence of basic sites of different strengths. Fig. 4 also reported that $La_2O_3$ addition
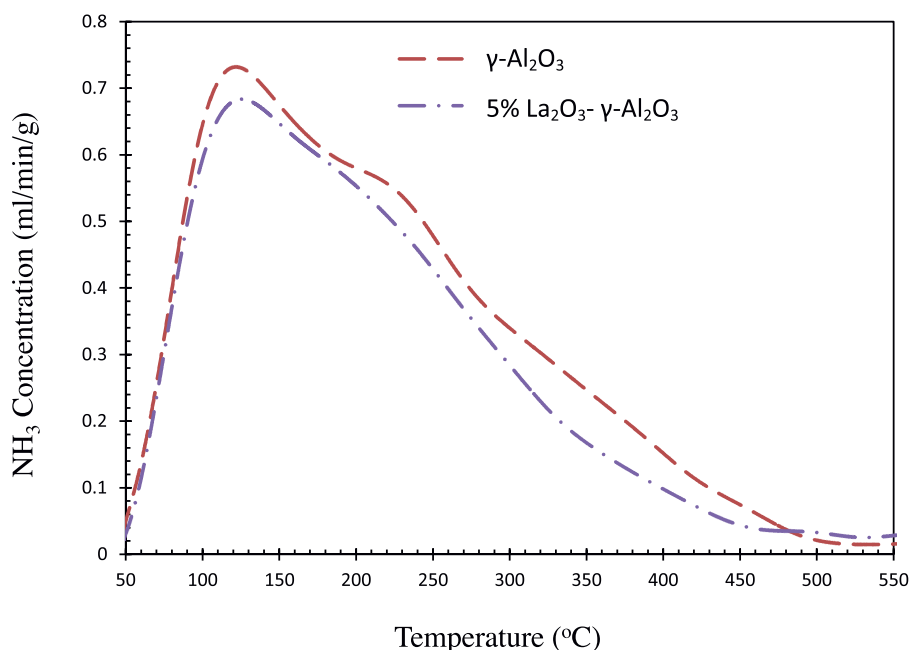
**Fig. 3.** NH$_3$-TPD profile of bare and La$_2$O$_3$ modified γ-Al$_2$O$_3$ samples.

significantly increases both the density and the strength of basic sites.

To study the influence of La$_2$O$_3$ loading on both acidity and basicity, NH$_3$ and CO$_2$ TPDs of γ-Al$_2$O$_3$ samples with different La$_2$O$_3$ content were performed. Regarding total acidity, one can notice in Table 2, that total acidity was decreased from 511 to 467 μmol NH$_3$/g γ-Al$_2$O$_3$ with the addition of 2 wt% La$_2$O$_3$. Furthermore, addition of the 5 wt% La$_2$O$_3$ yielded a further decrease in acidity. Fig. 5 report the concentration profiles of acidic and basic sites with the variation of La$_2$O$_3$ loadings on γ-Al$_2$O$_3$. As shown in Fig. 5, La$_2$O$_3$ loading beyond 5 wt% resulted in the gradual rise of acid

site concentrations. For example, acid site concentrations of 15 wt% La$_2$O$_3$- γ-Al$_2$O$_3$ were found to be equivalent to 2.84 μmol NH$_3$/m$^2$, whereas it was 2.39 μmol NH$_3$/m$^2$ for γ-Al$_2$O$_3$ modified with 5 wt% La$_2$O$_3$. This effect can be attributed to the presence of deficiently coordinated La$^{3+}$ ions acting as Lewis acid sites [39,41,54]. One should notice, in this respect, that La$^{3+}$ cations can mildly influence the acid site density.

La$_2$O$_3$ addition improved, on the other hand, the CO$_2$ adsorption capacity of γ-Al$_2$O$_3$ by creating basic sites. For the 2 wt% La$_2$O$_3$ loading, total basicity (CO$_2$ adsorption capacity) was increased from 116 to 129 μmol CO$_2$/g γ-Al$_2$O$_3$. As reported in Fig. 5, the increase
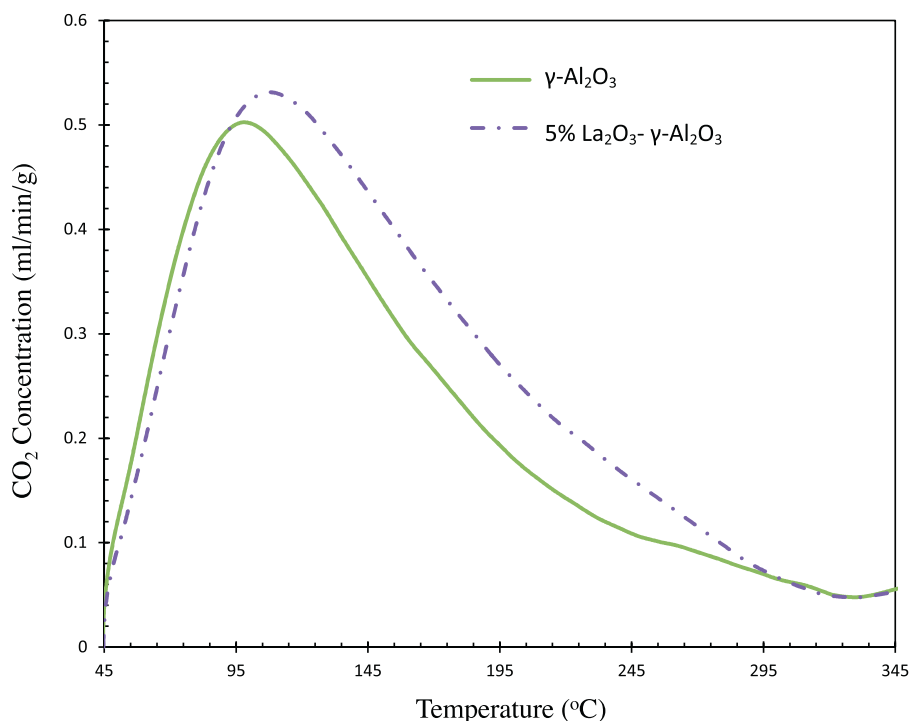


**Fig. 4.** CO$_2$-TPD profile of bare and La$_2$O$_3$ modified γ-Al$_2$O$_3$ samples.

**Table 2**
Total acidity and basicity of the bare and $La_2O_3$ modified $\gamma$-$Al_2O_3$ samples as determined from $NH_3$-TPD and $CO_2$-TPD, respectively.

| $La_2O_3$ loading (%) | Total acidity | | Total basicity | |
|---|---|---|---|---|
| | $\mu$mol/g $\gamma$-$Al_2O_3$ | $\mu$mol/m$^2$ | $\mu$mol/g $\gamma$-$Al_2O_3$ | $\mu$mol/m$^2$ |
| 0 | 511 | 2.84 | 116 | 0.65 |
| 2 | 467 | 2.51 | 129 | 0.70 |
| 5 | 458 | 2.39 | 170 | 0.88 |
| 10 | 464 | 2.60 | 261 | 1.46 |
| 15 | 471 | 2.84 | 313 | 1.90 |

in basic sites with $La_2O_3$ content is slow at low $La_2O_3$ loadings, as some of the $La_2O_3$ is employed to neutralize the acid sites of $\gamma$-$Al_2O_3$. Then, at higher $La_2O_3$ loadings, it starts to increase more progressively given the availability of free dispersed $La_2O_3$. However, as the $La_2O_3$ content becomes much higher, the rate of basicity increase with $La_2O_3$ content becomes modest. Lower surface areas and lower $La_2O_3$ dispersion at higher $La_2O_3$ loadings are likely to be responsible for this observed change. In agreement with this, Bettman et al. [40] also found that $La_2O_3$ remained in the dispersed phase up to a concentration of 8.5 $\mu$mol La/m$^2$ ($\sim$10 wt% La loading).

### 3.2. Effect of catalyst reduction conditions

Surface area loss of $\gamma$-$Al_2O_3$ at high temperatures can occur due to the following phenomena: (a) sintering via collapse of its pores and (b) phase transformation yielding $\alpha$-$Al_2O_3$ [31]. The sintering of particles is responsible for the surface area loss of $\gamma$-$Al_2O_3$ at temperatures below 1000 °C. At temperatures above 1000 °C, the phase transformation plays a major role in the $\gamma$-$Al_2O_3$ surface area loss. The addition of $La_2O_3$ improves the thermal resistance of $\gamma$-$Al_2O_3$ as shown in Section 3.1.1. Depending on the loading and calcination temperature, lanthanum is present as dispersed $La_2O_3$, crystalline $La_2O_3$ and $LaAlO_3$ [31,40,41,66–68]. At a lower loadings, lanthanum exists as a dispersed phase undetectable by XRD, reducing the $\gamma$-$Al_2O_3$ sintering. Depending on the specific surface area, there is a concentration limit to which $\gamma$-$Al_2O_3$ can accommodate dispersed lanthanum. Beyond this concentration limit, lanthanum can form crystalline $La_2O_3$ and $LaAlO_3$ on a $\gamma$-$Al_2O_3$ surface [31,40,41,66,68]. At temperatures above 1000 °C, lanthanum reacts with alumina to

form $LaAlO_3$ [31]. It was found using the XRD of lanthanum modified alumina, that the formation of $LaAlO_3$ occurred at 1000 °C in samples containing 5.8 wt% $La_2O_3$ [67] and 10 wt% $La_2O_3$ [68]. Beguin et al. [66] also reported the formation of $LaAlO_3$ on 11 wt% La/$Al_2O_3$ after calcination at 1050 °C. Thus, the formation of $LaAlO_3$ helps to retard the phase transformation of $\gamma$-$Al_2O_3$ when exposed to temperatures above 1000 °C. However, the surface area can be decreased due to pore blocking by the added $La_2O_3$ and $LaAlO_3$ formation. In the present study, surface area loss of $\gamma$-$Al_2O_3$ due to sintering is the main contributor to this phenomenon as both the catalyst preparation and the gasification experiments are conducted at temperatures below 700 °C. Furthermore, no evidence of phase transformation on the prepared catalysts was observed.

However, as reported in our previous study [56], formation of undesirable $LaAlO_3$ on a Ni/Alcan $\gamma$-$Al_2O_3$ catalyst containing 10 wt% $La_2O_3$ was detected by XRD (included in Fig. 6). To investigate the causes behind $LaAlO_3$ formation, XRDs of lanthanum modified $\gamma$-$Al_2O_3$ samples with different amounts of $La_2O_3$ were performed. For up to 5 wt% $La_2O_3$ loading, no $LaAlO_3$ peak was observed in the diffractograms of the $La_2O_3$/$\gamma$-$Al_2O_3$ even after calcination at 1100 °C. Fig. 6 also reports the XRD profiles of the fresh and calcined 10 wt% $La_2O_3$/Alcan $\gamma$-$Al_2O_3$ support. As shown in Fig. 6, $LaAlO_3$ formation was also not observed on freshly prepared 10 wt% $La_2O_3$/Alcan $\gamma$-$Al_2O_3$. In agreement with the literature [31,40,41,66–68], $LaAlO_3$ peaks on the 10 wt% $La_2O_3$/Alcan $\gamma$-$Al_2O_3$ support, were only observed after calcining the sample at 1000 °C for 8 h.

Furthermore, given that $LaAlO_3$ was not observed in the support (10 wt% $La_2O_3$/Alcan $\gamma$-$Al_2O_3$), it is hypothesized that these species could have been formed during Ni impregnation. In order to clarify
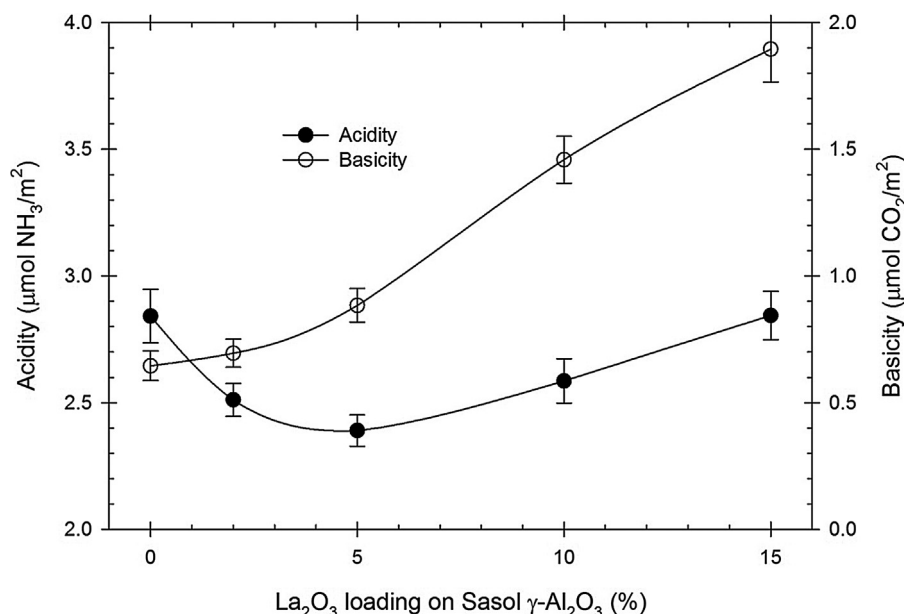


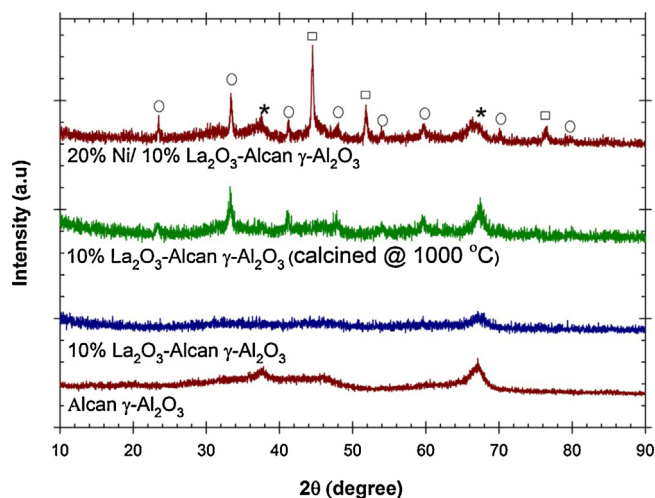**Fig. 5.** Effect of $La_2O_3$ loading on the acidity and basicity of the $\gamma$-$Al_2O_3$.
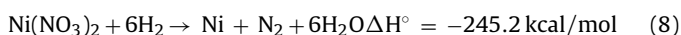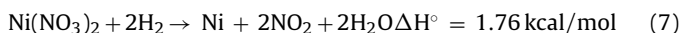
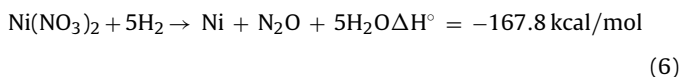**Fig. 6.** XRD patterns of 10 wt% $La_2O_3$ doped Alcan $\gamma$-$Al_2O_3$ samples. ($\star$: $\gamma$-$Al_2O_3$; $\square$: Ni; $\blacksquare$: NiO; $\bullet$: $NiAl_2O_4$; $\bigcirc$: $LaAlO_3$).

this matter one should consider the decomposition chemistry and thermodynamic of nickel nitrates under an $H_2$ atmosphere which involve the following reactions [69–71]:

$$Ni(NO_3)_2 + 9H_2 \rightarrow Ni + 2NH_3 + 6H_2O \, \Delta H^\circ = -267.32 \, \text{kcal/mol} \tag{4}$$

$$Ni(NO_3)_2 + 4H_2 \rightarrow Ni + 2NO + 4H_2O \, \Delta H^\circ = -86.5 \, \text{kcal/mol} \tag{5}$$

$$Ni(NO_3)_2 + 5H_2 \rightarrow Ni + N_2O + 5H_2O \, \Delta H^\circ = -167.8 \, \text{kcal/mol} \tag{6}$$

$$Ni(NO_3)_2 + 2H_2 \rightarrow Ni + 2NO_2 + 2H_2O \, \Delta H^\circ = 1.76 \, \text{kcal/mol} \tag{7}$$

$$Ni(NO_3)_2 + 6H_2 \rightarrow Ni + N_2 + 6H_2O \, \Delta H^\circ = -245.2 \, \text{kcal/mol} \tag{8}$$
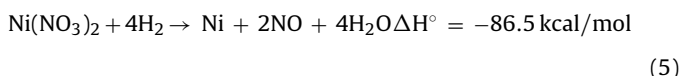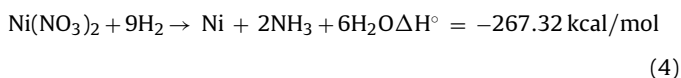
Eqs. (4)–(6) and (8) show that several highly exothermic reactions are involved in the nickel nitrate reduction. As a result, given the significant expected heat released, one can speculate that the reduction exothermicity is the main reason for $LaAlO_3$ formation with local temperatures surpassing 1000 °C. Failure to remove the evolved heat also results in excessive sintering. In fact, after Ni impregnation, a significant drop in the catalyst surface area was observed. Similar decomposition behavior was also reported for lanthanum nitrate [72]. Therefore, the flow during the catalyst reduction step becomes of crucial importance to control sintering since it carries out the evolved heat. In order to clarify this matter, 4 sets of catalysts were prepared using different reducing gas flows (based on the amount of nitrates): **NiLaA-LF**, **NiA-MF**, **NiLaA-MF** and **NiLaA-HF**.
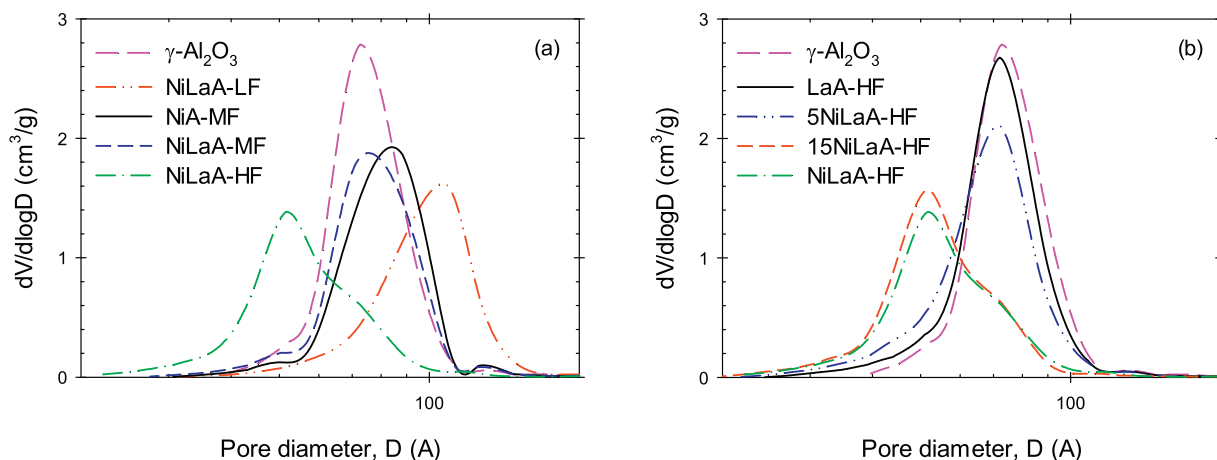
It is important to mention, that at low reducing gas flow (LF), the catalyst reduction chamber remained at fixed bed conditions. At medium reducing gas flow (MF), the catalyst bed was considered to be close to minimum fluidization. Finally, at high reducing gas flow (HF), intense fluidization with good heat distribution was achieved. Regarding the nitrate reduction rate, it has been reported that reactions are initiated as temperature approaches 270 °C [69]. The nitrate decomposition reaction can, however, be controlled by $H_2$ availability. In this respect, low reducing gas flows, while limiting the nitrate decomposition, also diminish the heat transfer across the bed very considerably. On the other hand, at a high reducing gas flow, nitrate decomposition may occur at faster rates; however, one can benefit from the overriding high heat transport and uniform bed temperatures. As a result of this, it can be anticipated that, low reducing gas flows lead to a significant rise of the local temperatures in the bed. In the following sections, the effect of the reducing gas flow rate on the textural properties, the Ni reducibility and dispersion, the acid–base properties, and the gasification performance of the catalysts are discussed.

### 3.2.1. Textural properties

Table 3 reports the BET surface area, the pore volume and the average pore diameter for both the support materials and Ni catalysts prepared by varying gas flow during the reduction of impregnated metal nitrates. The pore size distribution, as described in Fig. 7, was determined by analyzing the desorption branch of the isotherm and using the BJH (Barrett–Joyner–Halenda) method.

A major challenge in synthesizing Ni over $\gamma$-$Al_2O_3$ is to keep the porous structure of the support intact. In the catalyst preparation stage, the structure of the $\gamma$-$Al_2O_3$ support can be altered via thermal sintering and pore blocking when Ni is added. In this respect, the pore size distribution of $\gamma$-$Al_2O_3$ after 20 wt% Ni addition (NiA-MF) showed the evidence of blocking and the collapse of pores (Fig. 7(a)). Fig. 7(a) also shows that the addition of 5 wt% $La_2O_3$ (NiLaA-MF), helps to preserve the matrix structure improving its thermal resistance. The flow of the reducing gas can also play a major role in this regard, as shown in Table 3 and Fig. 7(a). Significant improvements in specific surface area of both the $La_2O_3$ modified $\gamma$-$Al_2O_3$ support and the supported Ni catalyst were found using a higher reducing gas flow rate. The $S_{BET}$ of a 20% Ni/5% $La_2O_3$-$\gamma$-$Al_2O_3$ was increased from 107 to 166 $m^2$/g by increasing reduction gas flow from 8 ml/mmol/min to 26 ml/mmol/min and from 2 ml/mmol/min to 12 ml/mmol/min, during lanthanum and nickel impregnation, respectively.

Table 3 also reports that, the average pore diameter of the samples was significantly decreased at higher reducing gas flows. It indicates the better dispersion of lanthanum and nickel in the $\gamma$-$Al_2O_3$ porous structure. Furthermore, pore size distribution of the samples, as shown in Fig. 7, can provide a better picture in this regard. For instance, the 20% Ni/5% $La_2O_3$-$\gamma$-$Al_2O_3$ catalyst prepared using low gas flow ( **NiLaA – LF**) displays a wide range of pore size distributions. This shows the blockage of smaller pores and the formation of larger pores due to sintering. With an increase in the reducing gas flow from 2 to 6 ml/mmol/min ( **NiLaA – MF**),

**Table 3**
BET surface area, pore volume and pore diameter of the supports and catalysts prepared by varying reduction flow rate.

| Samples | Reduction flow rate (ml/mmol/min) | $S_{BET}$ ($m^2$/g) | Pore volume ($cm^3$/g) | Avg pore dia (Å) |
|---|---|---|---|---|
| 5% $La_2O_3$-$\gamma$-$Al_2O_3$ ( **LaA – LF**) | 8 | 175 | 0.47 | 106 |
| 5% $La_2O_3$-$\gamma$-$Al_2O_3$ ( **LaA – MF**) | 16 | 183 | 0.48 | 104 |
| 5% $La_2O_3$-$\gamma$-$Al_2O_3$ ( **LaA – HF**) | 26 | 186 | 0.48 | 102 |
| 20%Ni/5%$La_2O_3$-$\gamma$-$Al_2O_3$ ( **NiLaA – LF**) | 2 | 107 | 0.33 | 124 |
| 20% Ni/$\gamma$-$Al_2O_3$ ( **NiA – MF**) | 6 | 128 | 0.39 | 113 |
| 20% Ni/5% $La_2O_3$-$\gamma$-$Al_2O_3$ ( **NiLaA – MF**) | 6 | 139 | 0.39 | 105 |
| 20% Ni/5% $La_2O_3$-$\gamma$-$Al_2O_3$ ( **NiLaA – HF**) | 12 | 166 | 0.32 | 76 |

**Fig. 7.** Pore size distribution based on desorption branch of (a) Ni catalysts prepared by varying the reduction gas flow and (b) **NiLaA – HF** at different loadings: 5% La$_2$O$_3$-γ-Al$_2$O$_3$ ( **LaA – HF**); 5% Ni/5% La$_2$O$_3$-γ-Al$_2$O$_3$ ( **5NiLaA – HF**); 15% Ni/5% La$_2$O$_3$-γ-Al$_2$O$_3$ ( **15NiLaA – HF**).

the sintering of pores was minimized. Pore size distribution of the catalyst prepared using high gas flow ( **NiLaA – HF**) showed better dispersion of nickel and lanthanum onto the γ-Al$_2$O$_3$ pores resulting in significantly higher specific surface area. Higher reducing gas flows can efficiently remove the heat evolved from the exothermic reactions. It can also quickly remove the water formed during nitrate decomposition. Moreover, higher reducing gas flows ensure uniform flow structure inside the catalyst reduction chamber. This could be another contributing factor for the better nickel dispersion onto the γ-Al$_2$O$_3$ pores. On the other hand, at a low reducing gas flow, gas channeling in the catalyst bed was observed. In this respect, the effect of the reduction gas flow on the catalyst structure is attributed to the exothermic decomposition of the metal nitrate precursor. This exothermic process, under limited heat removal, facilitates temperature runaway in the catalyst bed and thus leads to sintering.

### 3.2.2. X-ray diffraction analysis

XRD patterns of the fresh and used Ni catalysts prepared by varying the gas flow during the reduction of impregnated metal nitrates are reported in Fig. 8. Fig. 8 also presents the XRD pattern of the γ-alumina, showing a mostly amorphous structure. According to JCPDS 10-0425, the low intensity peaks centered at $2\theta = 37.6°$, $45.8°$, $67.1°$ are the characteristic peaks of γ-Al$_2$O$_3$.
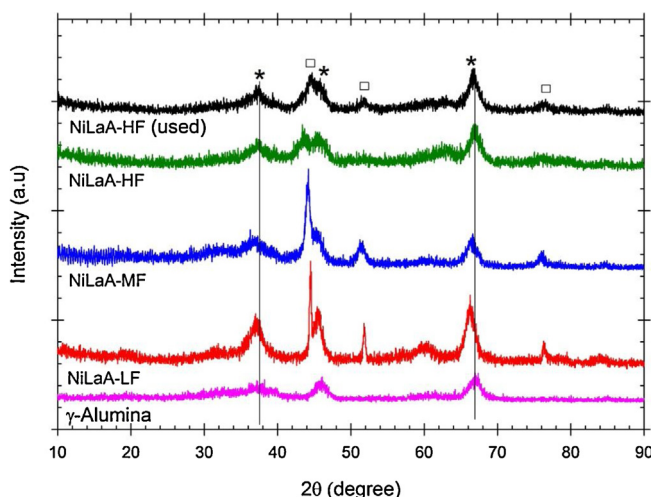


**Fig. 8.** XRD patterns of the fresh and used (in 2-methoxy-4-methylphenol gasification) Ni catalysts prepared by varying reduction gas flow. (★: γ-Al$_2$O$_3$; □: Ni).

As shown in Fig. 8, Ni catalysts (containing 20 wt% Ni on 5 wt% La$_2$O$_3$-γ-Al$_2$O$_3$ support) gave reflections of Ni (JCPDS 04-850) centered at $2\theta = 44.4°$, $51.8°$, $76.4°$. For the catalysts prepared with lower gas flow ( **NiLaA – LF** and **NiLaA – MF**), sharper and more intense Ni peaks were observed indicating the formation of larger Ni crystals. On the other hand, catalysts prepared with high reduction flow ( **NiLaA – HF**) gave broader Ni reflection peaks corresponding to well-dispersed small crystals on a thin layer of amorphous nickel species. This can be attributed to the better dispersion of Ni onto γ-Al$_2$O$_3$ pores as observed from the pore size distribution of **NiLaA – HF** (Fig. 7). For the purpose of comparison, the crystallite size of Ni is determined by applying the Scherrer equation (Eq. (3)). The broadening of the Ni (1 1 1) diffraction line at 45.4° was used to calculate the particle size. For the **NiLaA – LF** and **NiLaA – MF**, the average crystal sizes of Ni were found to be 21.3 and 13.1 nm, respectively. On the other hand, Ni crystallites of 5.5 nm size were formed on **NiLaA – HF**. The size of the Ni crystallites of **NiLaA – HF** after being used in the 15 consecutive cycles of 2-methoxy-4-methylphenol gasification remained essentially the same (5.7 nm). Furthermore, the XRD pattern of the used catalyst confirms the absence of graphitic carbon on the catalyst surface. This result suggests that this catalyst is stable for steam gasification of tars with negligible crystallite agglomeration.

Fig. 8 also shows that for the **NiLaA – LF** and **NiLaA – MF**, γ-Al$_2$O$_3$ diffraction lines were shifted, especially at $2\theta = 67.1°$. The alteration of the γ-Al$_2$O$_3$ structure, for the catalysts prepared with lower gas flow was also found in N$_2$ physisorption experiments, as discussed in Section 3.2.1. Moreover, the formation of amorphous like very small Ni crystallites on NiLaA-HF indicates that catalysts prepared using higher reducing gas flows possess stronger metal-support interactions. This metal-support interaction of the catalysts is investigated using temperature programmed reduction (TPR) in the next section.

### 3.2.3. Catalyst reducibility, dispersion and crystal size

Fig. 9 reports the TPR profiles of the catalysts prepared by varying the reducing gas flow. Ni reducibility ($R$), dispersion ($D$) and crystallite size ($d_v$) data as calculated from TPR and H$_2$ pulse chemisorptions are summarized in Table 4. Fig. 9(a), shows that the Ni (20 wt%) catalyst exhibits wide reduction peaks in the 300 °C–950 °C range with four peaks at around 380, 470, 610 and 780 °C. The first peak (at 380 °C) can be assigned to the reduction of highly dispersed NiO species on the support surface [73–75]. According to the technical literature [36,73,75–81], the second and third peaks can be attributed to the reduction of NiO in various states of interaction with the support. Interaction of Ni with
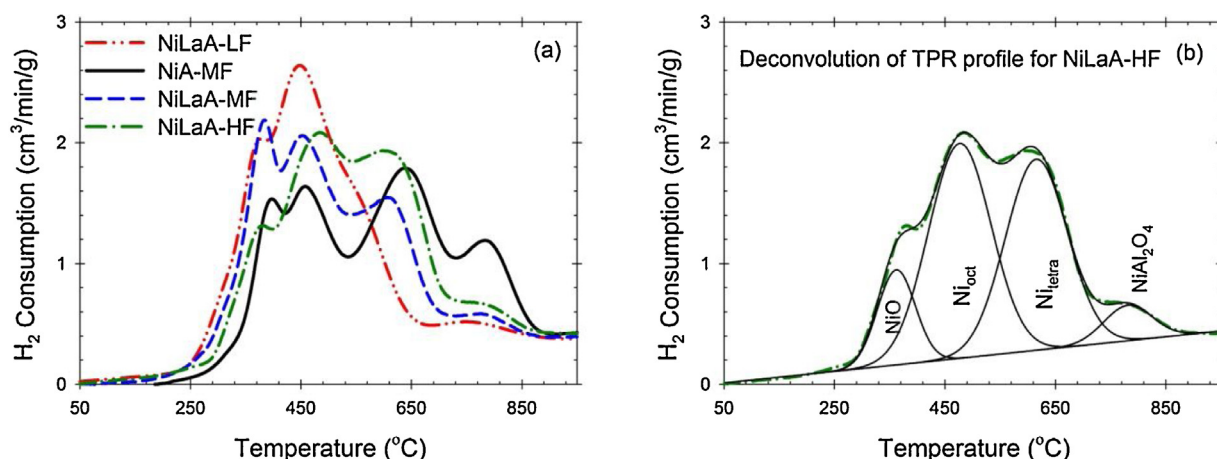
**Fig. 9.** (a) TPR profiles of the catalysts prepared by varying reduction gas flow and (b) deconvolution of the TPR profile for **NiLaA – HF**. (using 10% $H_2$ with balanced Ar at a flow rate of 50 cm$^3$/min and 10 °C/min heating rate).

the support leads to the formation of surface nickel–aluminate spinels on the interface of Ni/Al$_2$O$_3$. Moreover, γ-Al$_2$O$_3$ is a defective spinel phase of alumina with cation site vacancies randomly distributed throughout the crystal. Therefore, two types of surface spinels are anticipated to be formed by accommodating Ni ions in the tetrahedral and octahedral sites of alumina. Surface nickel aluminates that are reducible at 500 °C can be attributed to the Ni$^{2+}$ occupying octahedral sites of γ-Al$_2$O$_3$, whereas the unreducible species are referred to as Ni$^{2+}$ placed in the tetrahedral sites of γ-Al$_2$O$_3$ [78,79,82]. Finally, the reduction peak observed at 780 °C can be assigned to the reduction of bulk nickel–aluminate (NiAl$_2$O$_4$) [36,73–76,83].

Regarding TPR profiles, they also displayed differences in the relative proportion of Ni species with the variation of preparation conditions and La$_2$O$_3$ addition. In this respect, the relative proportion of Ni species was determined by deconvoluting TPR profiles using four Gaussian peaks, as shown in Fig. 9(b) for **NiLaA – HF**. Fig. 9(a) and Table 4, show that a decrease in the reducing gas flow from 12 ml/mmol nitrates/min ( **NiLaA – HF**) to 6 ml/mmol nitrates/min ( **NiLaA – MF**) yields a higher proportion of NiO and Ni$^{2+}$ in octahedral sites (Ni$_{oct}$) reducing the Ni$^{2+}$ occupying the tetrahedral sites of γ-Al$_2$O$_3$ (Ni$_{tetra}$). Furthermore, the comparison of TPR profiles between the unpromoted Ni/γ-Al$_2$O$_3$ catalyst ( **NiA – MF**) and the La$_2$O$_3$ promoted catalyst ( **NiLaA – MF**), prepared at same conditions, displayed increases in the reduction temperatures for all Ni species. **NiA – MF** also yielded a higher proportion of Ni species requiring higher reduction temperatures (Ni$_{tetra}$ and bulk NiAl$_2$O$_4$). This is attributed to the influence of La$_2$O$_3$ in decreasing nickel–alumina interaction [36,76,84]. Moreover, at lower loadings, La$_2$O$_3$ preferentially deposited on the tetrahedral Al$^{3+}$ sites resulting in the decrease of Al$^{3+}_{tetra}$/Al$^{3+}_{oct}$ ratio [52].

On the other hand, when the reducing gas flow was further decreased to 2 ml/mmol/min ( **NiLaA – LF**), the intensity of the Ni$_{oct}$ peak was augmented significantly, with the 3rd peak (which

was assigned to Ni$_{tetra}$) shifting from 610 to 555 °C. The effect of the reduction gas flow, on the relative proportion of Ni$^{2+}$ in octahedral and tetrahedral γ-Al$_2$O$_3$ sites, can again be explained given the temperature rise difference during catalyst precursor decomposition. Regarding the local temperature in the catalyst reduction chamber, it was found that low reducing gas flow could lead to temperature rises of up to 1000 °C. Least rise in local temperatures is occurred when using the high reducing gas flow (12 ml/mmol/min). This was also confirmed by the lesser degree of sintering, as shown in Section 3.2.1, on the catalyst prepared using the high gas flow ( **NiLaA – HF**).

Dehydroxylation of γ-Al$_2$O$_3$, during high temperature thermal treatment, has been considered as the main reason for the sintering. Due to the dehydroxylation, Al$^{3+}$ starts to move from the surface tetrahedral sites, to the vacant interstices of the bulk structure, in order to satisfy the valence requirements [59,85]. As the low reducing gas flow yields a maximum rise in local temperatures, it is expected that **NiLaA – LF** experiences a higher degree of dehydroxylation. Therefore, under this condition unstable tetrahedral Al$^{3+}$ is going to be almost completely removed from the surface. In other words, higher dehydroxylation reduces the metal-support interactions resulting in lower reduction temperatures. On the other hand, the catalyst prepared with high reducing gas flow, provides higher metal-support interaction and facilitates Ni dispersion (Table 4). However, further increase in gas flow could yield lower Ni reducibility and dispersion at temperatures below 700 °C.

### 3.2.4 Acid–base properties

Fig. 10 reports the IR spectra of the γ-Al$_2$O$_3$ calcined at 700 °C and the prepared Ni catalysts following pyridine adsorption and evacuation at 100 °C, in the spectral region of 1700–1400 cm$^{-1}$. For all the samples, no band at 1540 cm$^{-1}$ was observed. This indicates that there are no Brønsted acid sites available, which are strong enough to form pyridinium ions. On the other hand, the appearance of the "19b" band at 1448 cm$^{-1}$ and the "8a" bands at 1590–1635 cm$^{-1}$ in the DRIFT spectra demonstrates the

**Table 4**
Reducibility ($R$), dispersion ($D$) and crystal size ($d_v$) of Ni for different catalysts.

| Samples | NiO (%) | Ni$_{oct}$ (%) | Ni$_{tetra}$ (%) | NiAl$_2$O$_4$ (%) | $R$ (%) | $D(\%) = \frac{117X}{WR}$ | $d_v$(nm) $= \frac{97.1}{\%D}$ |
|---|---|---|---|---|---|---|---|
| **NiLaA-LF** | 16.8 | 50.6 | 24.8 | 7.8 | 93 | 2.88 | 34 |
| **NiA-MF** | 10.7 | 30.3 | 45.1 | 14.0 | 89 | 2.99 | 32 |
| **NiLaA-MF** | 19.2 | 44.7 | 29.3 | 6.8 | 94 | 3.53 | 28 |
| **NiLaA-HF** | 11.7 | 44.0 | 38.7 | 5.6 | 95 | 4.52 | 21 |

$X$ stands for the total hydrogen chemisorbed (mmol of $H_2$/g cat); $W$ denotes the metal loading (wt%).

**Table 5**
Total acidity and basicity of the La$_2$O$_3$ modified γ-Al$_2$O$_3$ supports and Ni catalyst prepared by varying reduction gas flow as determined from NH$_3$ and CO$_2$-TPD.

| Samples | Reduction flow rate (ml/mmol/min) | Total acidity (μmol/g γ-Al$_2$O$_3$) | Total basicity (μmol/g γ-Al$_2$O$_3$) |
|---|---|---|---|
| 5% La$_2$O$_3$-γ-Al$_2$O$_3$ (***LaA-LF***) | 8 | 435 | 168 |
| 5% La$_2$O$_3$-γ-Al$_2$O$_3$ (***LaA-MF***) | 16 | 458 | 179 |
| 5% La$_2$O$_3$-γ-Al$_2$O$_3$ (***LaA-HF***) | 26 | 476 | 195 |
| 20% Ni/5% La$_2$O$_3$-γ-Al$_2$O$_3$ (***NiLaA-LF***) | 2 | 415 | 115 |
| 20% Ni/γ-Al$_2$O$_3$ (***NiA-MF***) | 6 | 546 | 98 |
| 20% Ni/5% La$_2$O$_3$-γ-Al$_2$O$_3$ (***NiLaA-MF***) | 6 | 510 | 153 |
| 20% Ni/5% La$_2$O$_3$-γ-Al$_2$O$_3$ (***NiLaA-HF***) | 12 | 550 | 188 |
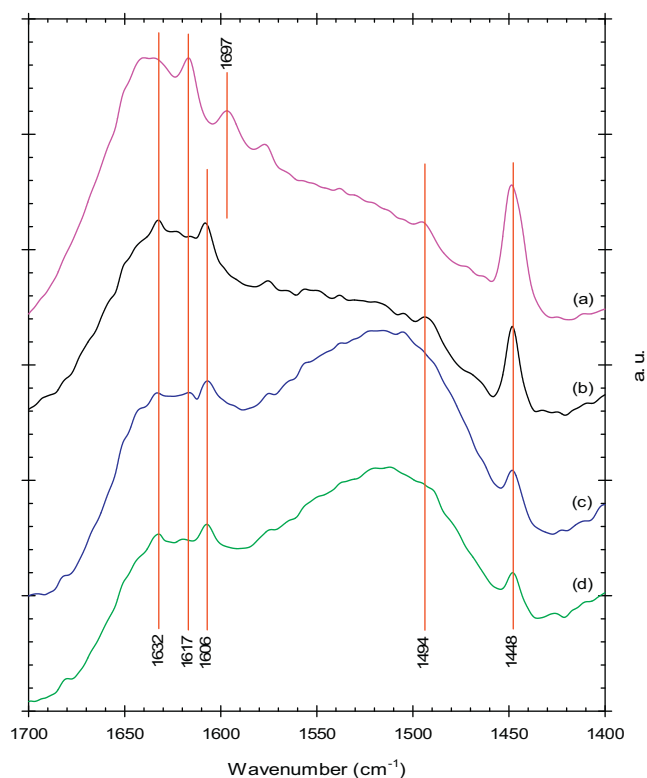


**Fig. 10.** Pyridine DRIFT spectra of (a) **γ-Al$_2$O$_3$**, (b) ***NiA – MF***, (c) ***NiLaA – MF***, and (d) ***NiLaA – HF***.

presence of Lewis acid sites. It can also be seen from Fig. 10 that the addition of 5 wt% La$_2$O$_3$ resulted in the reduction of intensity of the peak at 1448 cm$^{-1}$. This, once again confirms the role of La$_2$O$_3$ in decreasing Lewis acidity of γ-Al$_2$O$_3$.

The multiplicity of the "8a" band of coordinated pyridine, as shown in Fig. 10, demonstrates the presence of Lewis acid sites (Al$^{3+}$) in both octahedral and tetrahedral coordination [59,63,64]. Different configurations of Al$^{3+}$ in the γ-Al$_2$O$_3$ defect spinel, are shown in Fig. 11. Three types of Lewis acid sites with different strengths have been reported in the literature [59,62–64,86,87]: weak (1590–1610 cm$^{-1}$), moderate (1610–1620 cm$^{-1}$) and strong
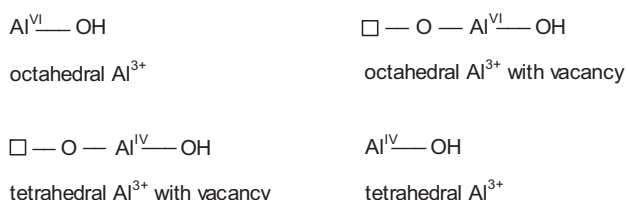


**Fig. 11.** Different configurations of Al$^{3+}$ in γ-Al$_2$O$_3$.

(1625–1635 cm$^{-1}$). The weak and strong Lewis sites correspond to five coordinated (quasi octahedral) and three coordinated (quasi tetrahedral) Al ions which are formed by dehydroxylation of octahedral and tetrahedral Al$^{3+}$, respectively. The moderate strength Lewis acid sites are attributed to four coordinated Al$^{3+}$ [64,86,87]. On the other hand, Morterra and Magnacca [59] assigned the moderate strength Lewis sites to the tetrahedral Al$^{3+}$ with a cation vacancy (□–O–Al$^{IV}$).

Pyridine DRIFT spectra of γ-Al$_2$O$_3$ exhibits peaks at 1597 cm$^{-1}$ and 1617 cm$^{-1}$ in the IR spectra (Fig. 10) indicating the presence of weak and moderate Lewis acid sites. The absence of pyridine coordination with tetrahedral Al$^{3+}$ (strong Lewis acid) suggests that an activation temperature in excess of 700 °C is required to expose those sites at the alumina surface [59,87]. On the other hand, Ni catalysts exhibited IR bands at 1606 and 1632 cm$^{-1}$ for pyridine co-ordinate with the unsaturated Al$^{3+}$ in octahedral and tetrahedral sites, respectively. The shift of the octahedral Al$^{3+}$ peak from 1697 (for γ-Al$_2$O$_3$) to 1606 cm$^{-1}$ indicates the increase of its strength after Ni impregnation. Furthermore, the absence of moderate strength sites on the Ni catalysts can be explained by the non-defective NiAl$_2$O$_4$ spinels formation on the catalyst surface at 20 wt% Ni loading.

The acidity and basicity of the catalysts were quantitatively investigated by temperature programmed desorption (TPD) of NH$_3$ and CO$_2$, respectively. Table 5 reports the total acidity and basicity of the La$_2$O$_3$ modified γ-Al$_2$O$_3$ supports and the Ni catalysts prepared varying the reducing gas flow. One can notice that there is a rise in acidity with the increase in reducing gas flow. This can be attributed to the lower thermal sintering (dehydroxylation) and to the higher specific surface area experienced when preparing these samples. On the other hand, the improvement in CO$_2$ adsorption/total basicity for both the supports and the Ni catalysts as shown in Table 5 and Fig. 12, indicates that higher reducing gas flow facilitate La$_2$O$_3$ dispersion.

Fig. 13(a) reports the NH$_3$-TPD profiles of the Ni catalysts prepared using different reducing gas flow rates. In agreement with the pyridine DRIFT spectra (Fig. 10), two peaks in the range of 50–500 °C were observed in the NH$_3$-TPD profiles of the Ni catalysts. According to Morterra and Magnacca [59], pyridine adsorbed on the weak Lewis sites (octahedral Al$^{3+}$) starts to desorb at ambient temperature, whereas evacuation of pyridine from tetrahedral Al$^{3+}$ sites requires more than 200 °C. Based on that, low and high temperature peaks in the NH$_3$-TPD profiles, can be assigned to the octahedral Al$^{3+}$ (weak) Lewis acid sites and tertrahedral Al$^{3+}$ (strong) Lewis acid sites, respectively.

Fig. 13(a) also reports that with the decrease in reducing gas flow, Al$_{tetra}^{3+}$ Lewis acid sites starts to diminish due to the greater extent of dehydoxylation as discussed in the previous sections. An increase in the amount of Al$_{oct}^{3+}$ Lewis acid sites was also observed at the same time. According to the technical literature [59,63,87], the amount of surface octahedral and tetrahedral sites are independent of each other, i.e., one does not form at the expense of the other. Thus, the findings of this study appear to be in apparent disagreement with the technical literature. However, one has to
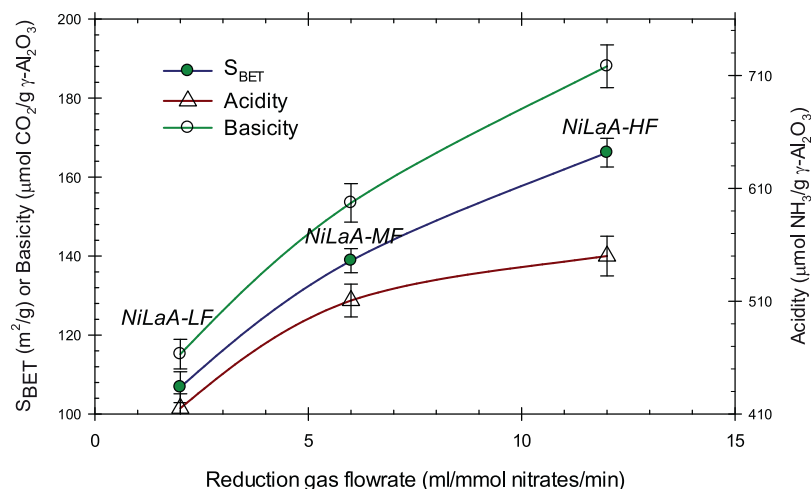
**Fig. 12.** $S_{BET}$, total acidity and basicity of the Ni catalysts prepared by varying reduction gas flow.

**Table 6**
Ratio of octahedral and tetrahedral $Al^{3+}$ sites.

| Samples | $H_2$ TPR $Ni_{oct}/Ni_{tetra}$ | $NH_3$ TPD $Al^{3+}_{oct}/Al^{3+}_{tetra}$ |
|---|---|---|
| *NiLaA-LF* | 2.04 | 1.97 |
| *NiA-MF* | 0.67 | 0.68 |
| *NiLaA-MF* | 1.52 | 1.47 |
| *NiLaA-HF* | 1.14 | 1.16 |

consider that changes in the relative proportion of $Al^{3+}_{oct}$ and $Al^{3+}_{tetra}$ can also be attributed to the $La_2O_3$ distribution over the octahedral and tetrahedral sites. It was observed, in this respect, that there was an improvement in $La_2O_3$ dispersion when using a higher reduction gas flow as shown by $CO_2$-TPD (Table 5). On the other hand, the difference in the TPD profiles of unpromoted (**NiA − MF**) and $La_2O_3$ promoted ( **NiLaA − MF**) catalysts, prepared using the same medium reducing gas flow, can be explained given the preferential neutralization of the tetrahedral Lewis acid sites resulting from $La_2O_3$ addition.

The relative proportion of $Al^{3+}_{oct}$ and $Al^{3+}_{tetra}$ was determined by deconvoluting the $NH_3$-TPD profiles, as shown in Fig. 13(b) for **NiLaA − HF**. It is interesting to note that the ratio of $Al^{3+}_{oct}$ and $Al^{3+}_{tetra}$ Lewis acid sites matches almost exactly the ratio of surface $NiAl_2O_4$ in the octahedral and tetrahedral configurations, as given in Table 6. It is hypothesized that the same octahedral and tetrahedral ratios were obtained from the both $H_2$-TPR and $NH_3$-TPD methods because of Ni loading beyond the monolayer coverage as

suggested by the NiO peak in the TPR profiles (Fig. 9(a)). Moreover, this finding confirms the applicability of classical $NH_3$-TPD and $H_2$ TPR techniques to efficiently determine the concentration of surface octahedral and tetrahedral $Al^{3+}$ sites in γ-$Al_2O_3$.

### 3.3. Gasification results

The performance of the Ni catalysts prepared using different gas flows during the catalyst reduction step was evaluated for the steam gasification of biomass surrogate species (glucose and 2-methoxy-4-methylphenol). Steam gasification experiments were performed in a CREC fluidized Riser Simulator at reaction temperature of 650 °C, catalyst/biomass ratio (Cat/B) of 12.5 g/g and reaction time of 20 s. Catalysts reactivity were compared in terms of the: (i) dry gas yield (moles of $H_2$, CO, $CO_2$ and $CH_4$ produced/moles of biomass fed), (ii) carbon conversion to permanent gases, (iii) quality of synthesis gas, (iv) coking, and (v) tars formed. Aromatics and oxygenates of $C_6^+$ structure in the produced gas were considered as tars. Experimental results were also compared to predicted chemical equilibrium data. Elevated reactor pressure after the conversion of biomass surrogate species in a constant volume CREC Riser Simulator was also considered to determine equilibrium under rigorous conditions. Coke and tars formations were also taken into account in the thermodynamic model.

Fig. 14 and Fig. 15 compare the performance of the Ni catalysts prepared by varying the reduction gas flow in terms of carbon conversion, dry gases yields and tar formation for glucose and
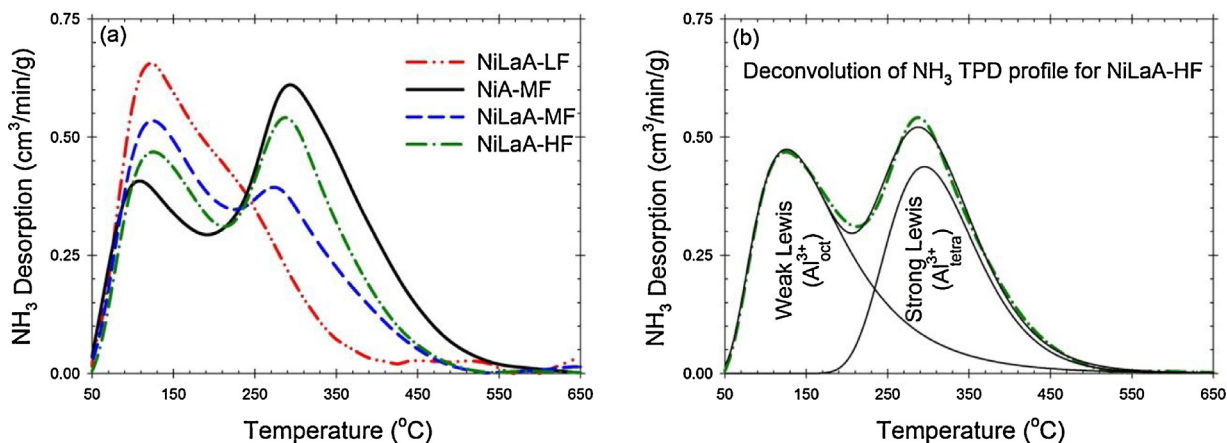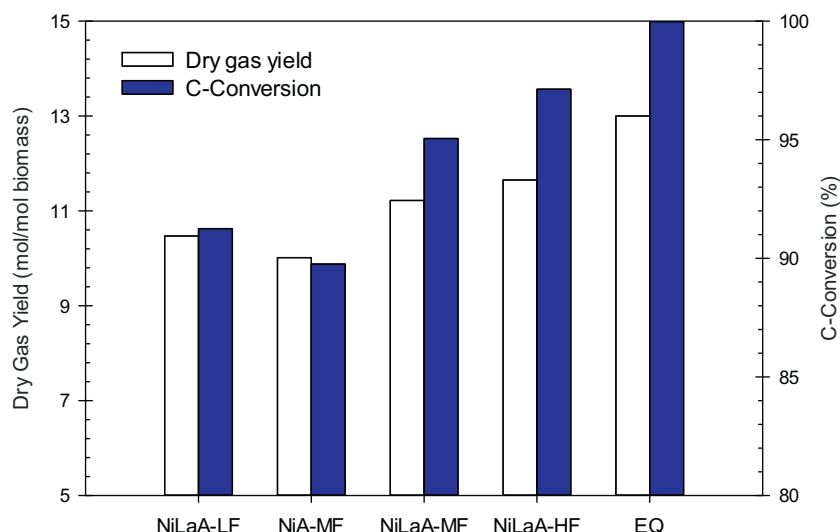


**Fig. 13.** (a) $NH_3$-TPD profiles of the catalysts prepared by varying gas flow at the catalyst reduction step and (b) deconvolution of the $NH_3$-TPD profile for **NiLaA − HF**.

**Fig. 14.** Dry gas yield and carbon-conversion during steam gasification of glucose at 650 °C, $S/B$ = 1.0 g/g, Cat/$B$ = 12.5 g/g, 20 s of reaction time using different catalysts: 20% Ni/$\gamma$-Al$_2$O$_3$ prepared using medium flow ( ***NiA – MF*** ), and 20% Ni/5% La$_2$O$_3$-$\gamma$-Al$_2$O$_3$ catalyst prepared using low flow ( ***NiLaA – LF***), medium flow ( ***NiLaA – MF*** ) and high flow ( ***NiLaA – HF***). EQ represents equilibrium data.
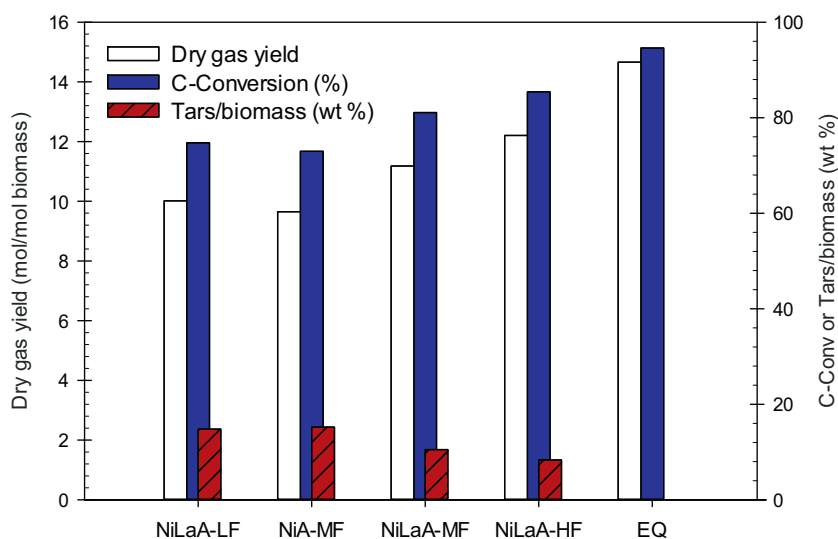
2-methoxy-4-methylphenol gasification, respectively. One can notice that 100% conversion of glucose was obtained without detectable tar formation at 650 °C and 20 s of reaction time. For the La$_2$O$_3$ modified Ni/$\gamma$-Al$_2$O$_3$ catalysts, a maximum of only 0.0014 g of coke deposition/g of catalyst was observed during glucose gasification.

On the other hand, it can be noticed in Fig. 15 that catalytic steam gasification of 2-methoxy-4-methylphenol yielded tars as well as higher amount of coke. This was assigned to the lower H/C and O/C ratios of 2-methoxy-4-methylphenol while compared to glucose. However, using the highly active catalyst developed in the present study, tars were kept as low as 8.3% at 650 °C. Moreover, XRD results of the catalyst used in 15 cycles of 2-methoxy-4-methylphenol gasification confirmed the absence of graphitic coke formation (Fig. 8).

Figs. 14–17 compare the gasification performance of unpromoted (***NiA-MF***) and La$_2$O$_3$ promoted (***NiLaA-MF***) Ni/$\gamma$-Al$_2$O$_3$ catalysts. These catalysts were prepared using the same gas flow during the catalyst reduction step. Significant improvement in carbon conversion and dry gas yield were, however, obtained

using the La$_2$O$_3$ promoted catalysts (***NiLaA-MF***) instead of the unprompted ***NiA-MF***. These findings were consistent for both glucose and 2-methoxy-4-methylphenol gasification. Regarding the role of La$_2$O$_3$ vis-a-vis steam and dry reforming, water gas shift and coke conversion were already discussed in our previous work [56].

The effect of catalyst reduction conditions on dry gas yield and carbon conversion from glucose gasification were reported in Fig. 14. This shows that, significant improvements in dry gas yield and carbon conversion can be achieved during glucose gasification using the catalysts prepared with higher gas flow at the catalyst reduction step. ***NiLaA – HF*** provides an example of this improvement, exhibiting a 97% conversion of carbon to permanent gases yielding 11.65 mol of dry gas per mole of glucose. One can also notice, as reported in Fig. 15, that differences in the performance of catalysts prepared by varying reduction gas flow are more significant in the case of 2-methoxy-methylphenol gasification. For instance, steam gasification of 2-methoxy-methylphenol using ***NiLaA – HF*** showed a 10% improvement in carbon conversion, a 21% enhancement in dry gas yield and a 5.3% reduction in



**Fig. 15.** Dry gas yield, carbon-conversion and tar yields of 2-methoxy-4-methylphenol steam gasification at 650 °C, $S/B$ = 1.5 g/g, Cat/B = 12.5 g/g, 20 s of reaction time using different catalysts. EQ represents equilibrium data.
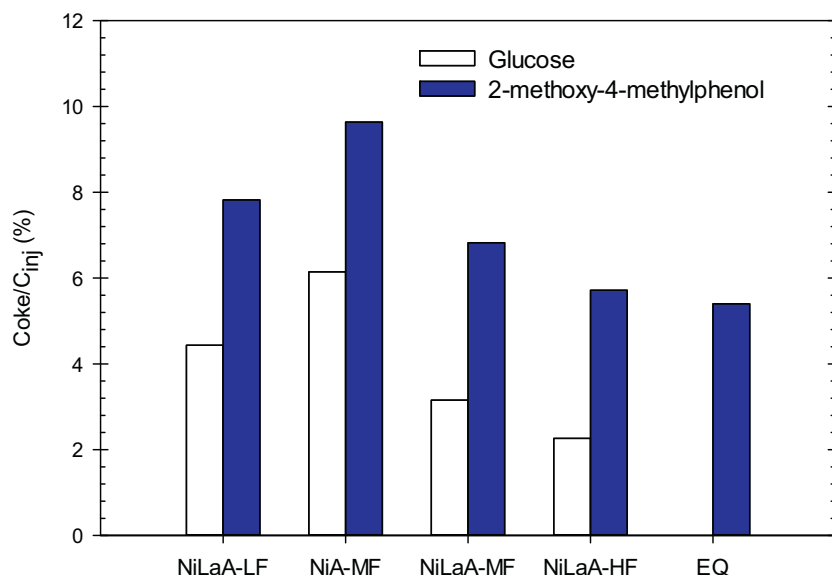
**Fig. 16.** Coke deposition during steam gasification of glucose and 2-methoxy-4-methylphenol at 650 °C, Cat/$B$ = 12.5 g/g, 20 s of reaction time using different catalysts. EQ represents equilibrium data.

tars when compared to **NiLaA – LF**. Fig. 16 and Fig. 17 also provide evidence of lower coking and higher $H_2/CO$ ratio for the catalysts prepared with the higher reduction gas flows.

It is well established that the dispersion of the active phase (Ni) is a crucial determinant of catalyst reactivity. Surface area, Ni reducibility and crystallite size are related to Ni dispersion. Total basicity and acidity are the two other independent properties of a $Ni/Al_2O_3$ catalyst. Regarding the influence of basicity, it has been reported that catalysts having a higher basicity support show stronger resistance to carbon fouling during steam and dry hydrocarbon reforming [26,27,88–92]. It is, thus, hypothesized that a basic support could improve the adsorption of acidic $CO_2$ and steam. Therefore, the coke deposited on the support acid sites and on the Ni surface could be removed, as a result of the Boudouard reaction ($C + CO_2 \leftrightarrow 2CO$) and the heterogeneous water-gas shift reaction ($C + H_2O \leftrightarrow H_2 + CO$).

Fig. 18 reports that carbon conversion and dry gas yield obtained using different catalysts are well correlated as a function of the

Ni dispersion and the basicity/acidity ratio. Carbon conversion depends on the coke/char reforming reactions ($C + H_2O \leftrightarrow H_2 + CO$; $C + CO_2 \leftrightarrow 2CO$ and $CH_4 \leftrightarrow C + 2H_2$). Besides char and tar reforming, steam and dry reforming of methane also play a significant role in determining the dry gas yield. Fig. 19 shows the coke and $CH_4$ yields obtained from glucose and 2-methoxy-4-methylphenol gasification using different catalysts. One can notice that **NiLaA – LF** and **NiA – MF** gave very close $CH_4$ yields. These catalysts also possess similar Ni dispersions. Therefore, it can be hypothesized that properties of the active phase play the major role on the extent of reforming reactions. On the other hand, coke deposition on the different catalysts, indicates that properties of the support (basicity/acidity ratio) are important factors determining the extent of coke/char reforming.

Thus, it is demonstrated that catalyst reduction conditions have a significant influence on catalyst properties. Higher reduction gas flow resulted in reduced sintering, higher Ni and $La_2O_3$ dispersions, and improved basicity. Hence, it yielded higher biomass
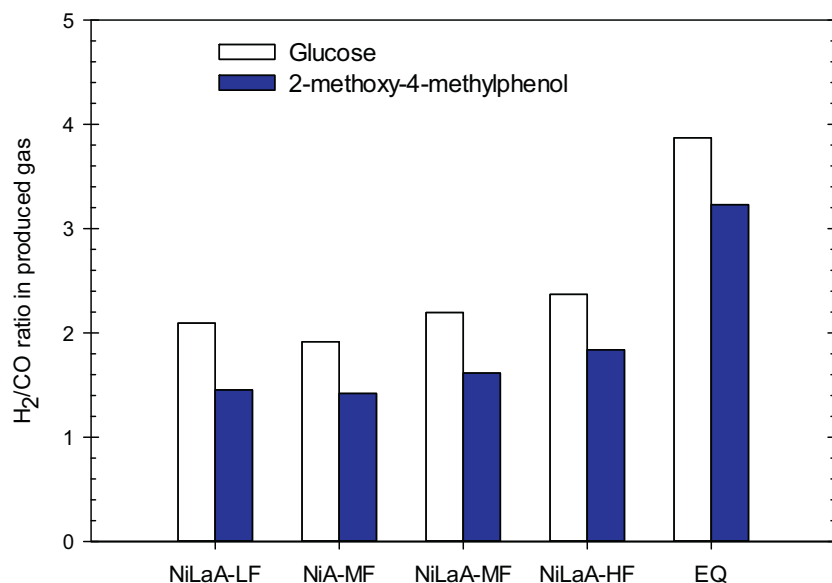


**Fig. 17.** $H_2/CO$ ratio in the products from steam gasification of glucose and 2-methoxy-4-methylphenol at 650 °C, Cat/$B$ = 12.5 g/g, 20 s of reaction time using different catalysts. EQ represents equilibrium data.
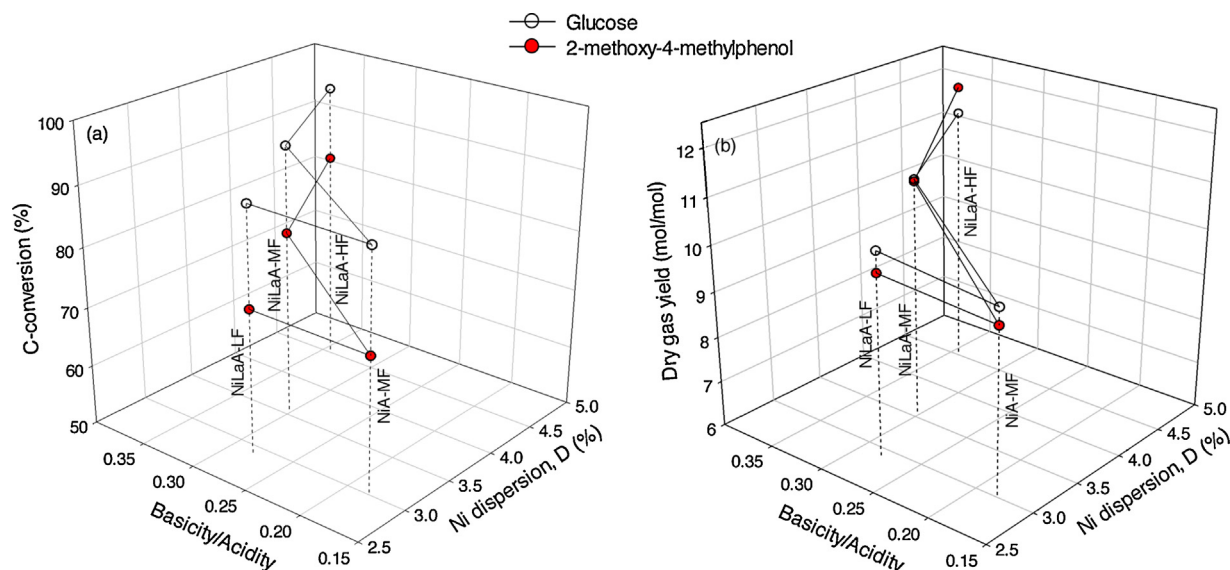
**Fig. 18.** Plot of (a) carbon conversion to permanent gases and (b) dry gas yield obtained during steam gasification of glucose and 2-methoxy-4-methylphenol, as a function of Ni dispersion (D) and basicity/acidity ratio.

steam gasification performance. It is proven that the fluidizable 20% Ni/5% La$_2$O$_3$-γ-Al$_2$O$_3$ catalyst ( **NiLaA – HF**) prepared using high reduction gas flow is able to gasify surrogate biomass species performing very close to thermodynamic chemical equilibrium. However, excessive increase in reducing gas flow may result in reduced Ni reducibility and limited dispersion (especially below 700 °C) by increasing metal-support interaction.

### 3.4. Catalyst stability

Catalystic biomass gasification may involve repeated oxidation–reduction cycles in both the gasifier and the catalyst regeneration units. To investigate the stability of the prepared catalysts under repeated oxidation–reduction cycles, successive TPO and TPR experiments were developed. Each cycle was composed of successive TPO, TPR, and pulse chemisorption experiments. Fig. 20 reports Ni reducibility, dispersion and crystallite size of **NiLaA – HF** under repeated oxidation and reduction cycles.

It can be observed in Fig. 20 that the 20% Ni/5% La$_2$O$_3$-γ-Al$_2$O$_3$ catalyst prepared using high reduction gas flow ( **NiLaA – HF**) showed stable reducibility in repeated oxidation–reduction cycles with an average reduction percentage of 94.8%. Pulse chemisorption results further confirm the stability and negligible metal crystallite agglomeration of the catalyst over repeated oxidation–reduction conditions with consistent percentage dispersion and crystal size of Ni.

Furthermore, to investigate the stability of **NiLaA – HF** in a biomass gasifier, multiple cycles gasification experiments were performed in the CREC Riser Simulator. Using **NiLaA – HF**, 35 cycles of glucose gasification at 650 °C were conducted with a 1.0 g/g steam/biomass ratio, a 12.5 g/g catalyst/biomass ratio and 20 s of reaction time in each cycle, without catalyst regeneration in between. Glucose gasification products after a random number of cycles were analyzed. Fig. 21 reports the carbon conversion to permanent gases obtained under the multiple cycles of steam gasification of glucose. **NiLaA – HF** showed stable glucose gasification performance over the cycles without significant deactivation. This result indicates that **NiLaA – HF** can be used efficiently for glucose gasification without requiring frequent catalyst regeneration.

The performance of the **NiLaA – HF** catalyst was also evaluated for 15 cycles of 2-methoxy-4-methylphenol gasification runs through consecutive reaction and regeneration cycles. In each cycle, 2-methoxy-4-methylphenol gasification was performed for 20 s at 650 °C, with a 1.5 g/g of steam/biomass ratio using a catalyst/biomass ratio of 12.5 g/g. After each gasification run, catalysts were regenerated in-situ. During the regeneration cycle, deposited coke was burned by utilizing a O$_2$/He mixture and reduced by using a H$_2$/Ar mixture. Fig. 22 shows the carbon conversion to permanent gases obtained during successive steam gasification of 2-methoxy-4-methylphenol runs. Fig. 22 reports that consistent 2-methoxy-4-methylphenol conversion can be achieved over successive gasification cycles using the **NiLaA – HF** catalyst. The absence
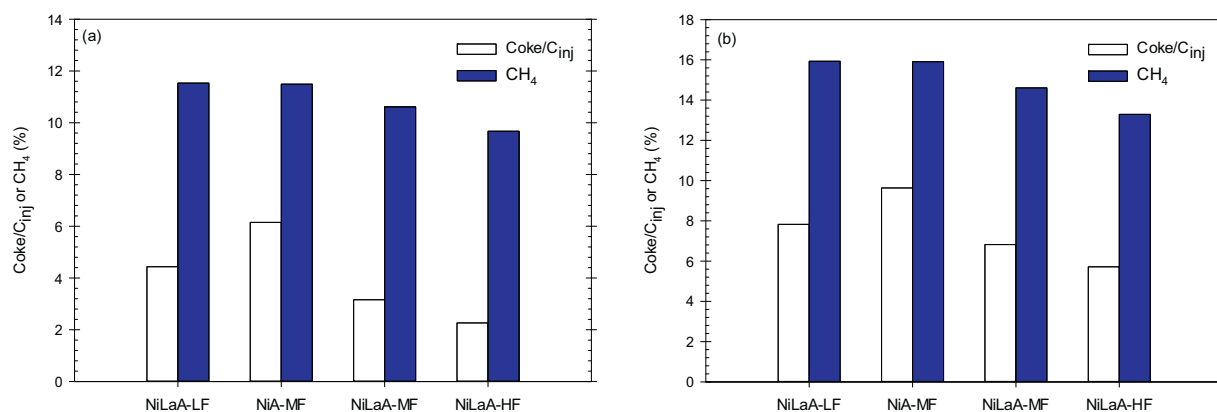


**Fig. 19.** Coke deposition and CH$_4$ yield obtained during steam gasification of (a) glucose and (b) 2-methoxy-4-methylphenol using different catalysts.
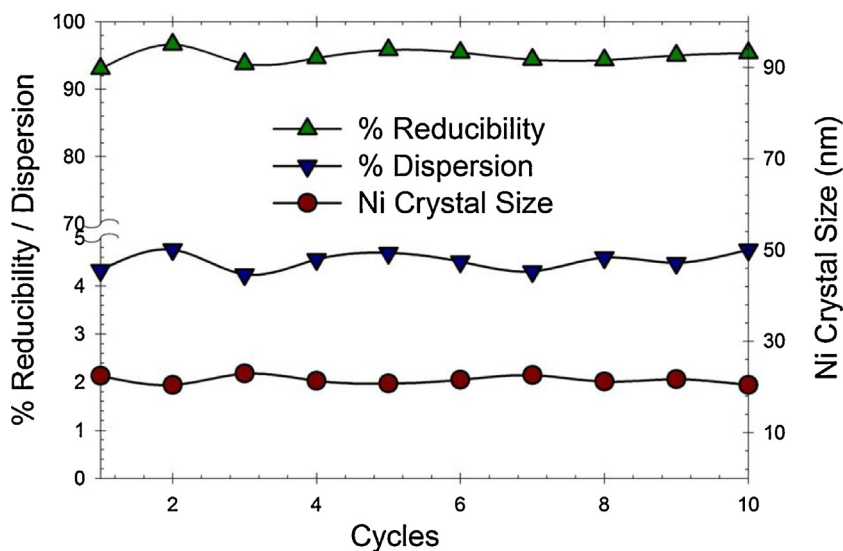
**Fig. 20.** Reducibility, dispersion and crystal size of **NiLaA – HF** over TPO/TPR cycles. (oxidizing agent: 5% $O_2$ in He; reducing agent: 10% $H_2$ in Ar; flow rate: 50 cm³/min; heating rate: 10 °C/min).
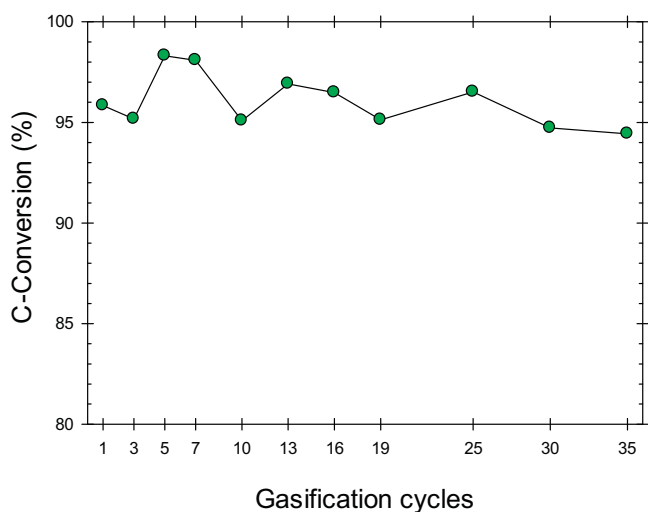


**Fig. 21.** Carbon conversion to permanent gases obtained during multiple cycles (without catalyst regeneration) of steam gasification of glucose at 650 °C, $S/B$ = 1.0 g/g, Cat/$B$ = 12.5 g/g and 20 s of reaction cycle using **NiLaA – HF**.
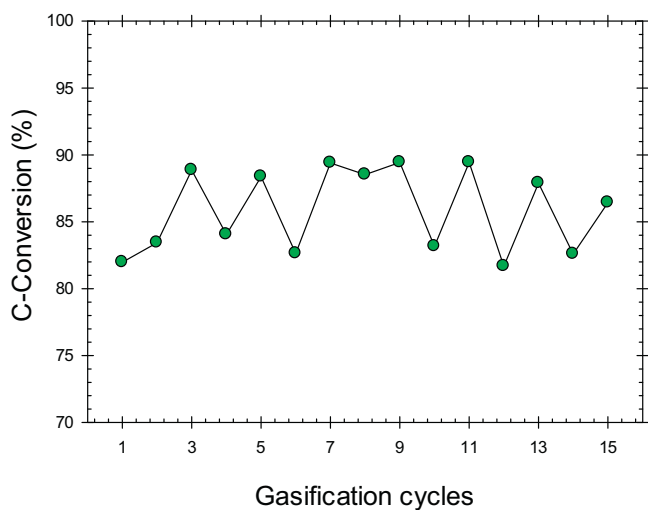


**Fig. 22.** Carbon conversion to permanent gases obtained during successive steam gasification runs of 2-methoxy-4-methylphenol at 650 °C, using a $S/B$ = 1.5 g/g, a Cat/$B$ = 12.5 g/g and a 20 s of reaction cycle with catalyst regeneration in between.

of graphitic coke deposition on this used catalyst, as shown in Fig. 8, makes the regeneration of this catalyst easy. Moreover, Fig. 20 showed the stability of the catalyst for repeated oxidation and reduction cycles. These results confirm the stability and regeneration ability of the **NiLaA – HF** catalyst for 2-methoxy-4-methylphenol gasification.

## 4. Conclusions

a) A fluidizable $La_2O_3$ promoted Ni/Sasol γ-$Al_2O_3$ catalyst, designated as **NiLaA-HF**, was developed. This catalyst is able to gasify 100% glucose without detectable tars formed at 650 °C. At the same temperature, gasification of methoxy-4-methylphenol yields 85.5% carbon conversion to permanent gases with only 8.3% tar formation and 5.7% carbon deposition as coke.

b) The developed **NiLaA – HF** catalyst performs close to the thermodynamic equilibrium, yielding a high-quality synthesis gas ($H_2$/CO ratio > 2.0). This catalyst also shows excellent stability under repeated gasification and regeneration cycles which are the expected operating conditions of a circulating fluidized bed gasifier.

c) The $La_2O_3$ addition, up to 5 wt%, helps to reduce thermal sintering and Lewis acidity of the γ-$Al_2O_3$ support as well as improved its basicity. Furthermore, controlled $La_2O_3$ addition, secures a positive impact on acid–base properties, and limits pore blocking. Moreover, 5 wt% $La_2O_3$ addition, contributes to higher Ni dispersion and to a high abundance of easily reducible species. Excessive $La_2O_3$ addition facilitates undesirable $LaAlO_3$ formation with Ni crystallite agglomeration and active sites blocking.

d) The catalyst precursor reduction step has to be carefully considered to prevent local bed temperatures from rising. This is critical due to the exothermicity of the metal nitrate reduction reaction. The bed temperature may be responsible for severe catalyst sintering via γ-$Al_2O_3$ dehydroxylation.

e) The gas flow rate during catalyst reduction plays an important role on acid–base properties, metal dispersion and crystal size. Higher reduction gas flow helps to maintain the structure of the γ-$Al_2O_3$ (a transitional phase of alumina) by removing heat from the exothermic nitrate reduction. This also yields improved metal dispersion. On the other hand, excessive reduction gas flow may lead to a lessened Ni reducibility.

f) The relative proportion of octahedral and tetrahedral sites in γ-$Al_2O_3$ is a significant indicator of its potential dehydroxylation.

This relevant parameter is estimated, in this study, using $NH_3$-TPD and $H_2$ TPR techniques.

## Acknowledgements

## References

[1] X.T. Li, J.R. Grace, C.J. Lim, a. P. Watkinson, H.P. Chen, J.R. Kim, Biomass Bioenergy 26 (2004) 171–193.
[2] P. McKendry, Bioresour. Technol. 83 (2002) 47–54.
[3] V. Kirubakaran, V. Sivaramakrishnan, R. Nalini, T. Sekar, M. Premalatha, P. Subramanian, Renew. Sustain. Energy Rev. 13 (2009) 179–186.
[4] B. Hejazi, J.R. Grace, X. Bi, A. Mahecha-Botero, Fuel 117 (2014) 1256–1266.
[5] L. Devi, K.J. Ptasinski, F.J.J.G. Janssen, Biomass Bioenergy 24 (2003) 125–140.
[6] M. Asadullah, Renew. Sustain. Energy Rev. 29 (2014) 201–215.
[7] M. Balat, Energy Sources Part A Recovery Util. Environ. Eff. 31 (2009) 516–526.
[8] A.V. Bridgwater, Fuel 74 (1995) 631–653.
[9] H.I. de Lasa, E. Salaices, J. Mazumder, R. Lucky, Chem. Rev. 111 (2011) 5404–5433.
[10] L. Wang, C.L. Weller, D.D. Jones, M.A. Hanna, Biomass Bioenergy 32 (2008) 573–581.
[11] P. McKendry, Bioresour. Technol. 83 (2002) 55–63.
[12] P. Parthasarathy, K.S. Narayanan, Renew. Energy 66 (2014) 570–579.
[13] J. Udomsirichakorn, P.A. Salam, Renew. Sustain. Energy Rev. 30 (2014) 565–579.
[14] A.V. Bridgwater, Chem. Eng. J. 91 (2003) 87–102.
[15] E. Salaices, B. Serrano, H.I. de Lasa, Ind. Eng. Chem. Res. 49 (2010) 6834–6844.
[16] D. Sutton, B. Kelleher, J.R.H. Ross, Fuel Process. Technol. 73 (2001) 155–173.
[17] A.V. Bridgwater, Appl. Catal. A Gen. 116 (1994) 5–47.
[18] J. Han, H. Kim, Renew. Sustain. Energy Rev. 12 (2008) 397–416.
[19] S. Nanda, P. Mohanty, K.K. Pant, S. Naik, J. a. Kozinski, A.K. Dalai, BioEnergy Res. 6 (2012) 663–677.
[20] L. Garcia, A. Benedicto, E. Romeo, M.L. Salvador, J. Arauzo, R. Bilbao, Energy Fuels 16 (2002) 1222–1230.
[21] E. Gusta, A.K. Dalai, M.A. Uddin, E. Sasaoka, Energy Fuels 23 (2009) 2264–2272.
[22] Z. Abu El-Rub, E.A. Bramer, G. Brem, Ind. Eng. Chem. Res. 43 (2004) 6911–6919.
[23] E.G. Baker, L.K. Mudge, M.D. Brown, Ind. Eng. Chem. Res. 26 (1987) 1335–1339.
[24] J. Ashok, S. Kawi, Int. J. Hydrogen Energy 38 (2013) 13938–13949.
[25] P. Lan, Q.-L. Xu, L.-H. Lan, D. Xie, S.-P. Zhang, Y.-J. Yan, Energy Sources Part A Recovery Util. Environ. Eff. 34 (2012) 2004–2015.
[26] L. Garcia, R. French, S. Czernik, E. Chornet, Appl. Catal. A Gen. 201 (2000) 225–239.
[27] R. Martínez, E. Romeo, L. García, R. Bilbao, Fuel Process. Technol. 85 (2003) 201–214.
[28] K. Tomishige, T. Kimura, J. Nishikawa, T. Miyazawa, K. Kunimori, Catal. Commun. 8 (2007) 1074–1079.
[29] A. Iriondo, V.L. Barrio, J.F. Cambra, P.L. Arias, M.B. Güemez, R.M. Navarro, M.C. Sanchez-Sanchez, J.L.G. Fierro, Catal. Commun. 10 (2009) 1275–1278.
[30] S. Bona, P. Guillen, J. Alcalde, L. Garcia, R. Bilbao, Chem. Eng. J. 137 (2008) 587–597.
[31] X. Chen, Y. Liu, G. Niu, Z. Yang, M. Bian, A. He, Appl. Catal. A Gen. 205 (2001) 159–172.
[32] F. Oudet, P. Courtine, A. Vejux, J. Catal. 114 (1988) 112–120.
[33] H. Schaper, E.B.M. Doesburg, P.H.M. de Korte, L.L. van Reijen, Solid State Ionics 16 (1985) 261–265.
[34] R. Yang, X. Li, J. Wu, X. Zhang, X. Xi, Z. Zhang, Catal. Lett. 132 (2009) 275–280.
[35] Q. Xu, P. Lan, B. Zhang, Z. Ren, Y. Yan, Energy Sources Part A Recovery Util. Environ. Eff. 35 (2013) 848–858.
[36] M. Sanchez-Sanchez, R. Navarro, J. Fierro, Catal. Today 129 (2007) 336–345.
[37] H. Cheng, X. Lu, Y. Zhang, W. Ding, Energy Fuels 23 (2009) 3119–3125.
[38] B. Valle, A. Remiro, A.T. Aguayo, J. Bilbao, A.G. Gayubo, Int. J. Hydrogen Energy 38 (2013) 1307–1318.
[39] R. Alvero, A. Bernal, I. Carrizosa, A. Odriozola, Inorg. Chim. Acta 140 (1987) 45–47.
[40] M. Bettman, R.E. Chase, K. Otto, W.H. Weber, J. Catal. 117 (1989) 447–454.
[41] L.P. Haack, J.E. deVries, K. Otto, M.S. Chattha, Appl. Catal. A Gen. 82 (1992) 199–214.
[42] R. Yang, X. Li, J. Wu, X. Zhang, Z. Zhang, J. Phys. Chem. C 113 (2009) 17787–17794.
[43] C. Cerritos, R.F. Ramírez, A.F.A. Alvarado, J.M.M. Rosales, V. García, I.R.G. Esquivel, Ind. Eng. Chem. Res. 50 (2011) 2576–2584.
[44] Y. Cui, H. Zhang, H. Xu, W. Li, Appl. Catal. A Gen. 331 (2007) 60–69.
[45] P. Kumar, Y. Sun, R.O. Idem, Energy Fuels 22 (2008) 3575–3582.
[46] Z.-W. Liu, H.-S. Roh, K.-W. Jun, J. Ind. Eng. Chem. 9 (2003) 267–274.
[47] S. Natesakhawat, O. Oktar, U.S. Ozkan, J. Mol. Catal. A Chem. 241 (2005) 133–146.
[48] S.-S. Lim, H.-J. Lee, D.-J. Moon, J.-H. Kim, N.-C. Park, J.-S. Shin, Y.-C. Kim, Chem. Eng. J. 152 (2009) 220–226.
[49] M. Scheithauer, H. Knozinger, M.A. Vannice, J. Catal. 705 (1998) 701–705.
[50] A. Slagtern, U. Olsbye, R. Blom, I.M. Dahl, H. Fjellvag, Appl. Catal. A Gen. 165 (1997) 379–390.
[51] X. Junke, Z. Wei, W. Jihui, L. Zhaojing, M. Jianxin, Chin. J. Catal. 30 (2009) 1076–1084.
[52] G. Del Angel, C. Guzmán, G. a. Bonilla, Torres, J.M. Padilla, Mater. Lett. 59 (2005) 499–502.
[53] G. Del Angel, Y. a. Bonilla, Peña, J. Navarrete, J.L.G. Fierro, D.R. Acosta, J. Catal. 219 (2003) 63–73.
[54] Y. Zhang, Y. Zhou, H. Liu, Y. Wang, Y. Xu, P. Wu, Appl. Catal. A Gen. 333 (2007) 202–210.
[55] J. Mazumder, H. de Lasa, Appl. Catal. B Environ. 160–161 (2014) 67–79.
[56] J. Mazumder, H.I. de Lasa, Catal. Today 237 (2014) 100–110.
[57] H.I. de Lasa, Riser Simulator, US Patent 5,10,2628,1992.
[58] E.P. Parry, J. Catal. 2 (1963) 371–379.
[59] C. Morterra, G. Magnacca, Catal. Today 27 (1996) 497–532.
[60] A.A. Khaleel, K.J. Klabunde, Chem. – A Eur. J. 8 (2002) 3991–3998.
[61] V. La Parola, G. Deganello, S. Scirè, A.M. Venezia, J. Solid State Chem. 174 (2003) 482–488.
[62] C. Morterra, S. Coluccia, A. Chiorino, F. Boccuzzi, J. Catal. 54 (1978) 348–364.
[63] C. Morterra, A. Chiorino, G. Ghiotti, E. Garrone, J. Chem. Soc. Faraday Trans. 1 75 (1979) 271–288.
[64] X. Liu, R.E. Truitt, J. Am. Chem. Soc. 119 (1997) 9856–9860.
[65] C. Morterra, A. Zecchina, S. Coluccia, A. Chiorino, J. Chem. Soc. Faraday Trans. 1 73 (1977) 1544–1560.
[66] B. Beguin, E. Garbowski, M. Primet, Appl. Catal. 75 (1991) 119–132.
[67] N.E. Bogdanchikova, S. Fuentes, M. Avalos-Borja, M.H. Farias, A. Boronin, G. Diaz, Appl. Catal. B Environ. 17 (1998) 221–231.
[68] L. Wachowski, P. Kirszensztejn, R. Łopatka, B. Czajka, Mater. Chem. Phys. 37 (1994) 29–38.
[69] C.H. Bartholomew, R.J. Farrauto, J. Catal. 45 (1976) 41–53.
[70] B. Jang, M. Helleson, C. Shi, A. Rondinone, V. Schwartz, C. Liang, S. Overbury, Top. Catal. 49 (2008) 145–152.
[71] S. Yuvaraj, L. Fan-yuan, C. Tsong-huei, Y. Chuin-tih, J. Phys. Chem. 107 (2003) 1044–1047.
[72] S. Mentus, D. Jeli, V. Grudi, J. Therm. Anal. Calorim. 90 (2007) 393–397.
[73] M.C. Alvarez-Galvan, R.M. Navarro, F. Rosa, Y. Briceño, F.G. Alvarez, J.L.G. Fierro, Int. J. Hydrogen Energy 33 (2008) 652–663.
[74] Y. Jilei, L. Zengxi, D. Huachao, L. Yuan, J. Rare Earths 24 (2006) 302–308.
[75] R.M. Navarro, M.C. Álvarez-Galván, F. Rosa, J.L.G. Fierro, Appl. Catal. A Gen. 297 (2006) 60–72.
[76] M. Sanchez-Sanchez, R. Navarro, J. Fierro, Int. J. Hydrogen Energy 32 (2007) 1462–1471.
[77] V. Gonzalezdelacruz, J. Holgado, R. Pereniguez, A. Caballero, J. Catal. 257 (2008) 307–314.
[78] F.-W. Chang, M.-S. Kuo, M.-T. Tsay, M.-C. Hsieh, J. Chem. Technol. Biotechnol. 79 (2004) 691–699.
[79] M. Wu, D.M. Hercules, J. Phys. Chem. 83 (1979) 2003–2008.
[80] G. Li, L. Hu, J.M. Hill, Appl. Catal. A Gen. 301 (2006) 16–24.
[81] B. Valle, B. Aramburu, A. Remiro, J. Bilbao, A.G. Gayubo, Appl. Catal. B Environ. 147 (2014) 402–410.
[82] J. Choi, S. Zhang, J.M. Hill, Catal. Sci. Technol. 2 (2012) 179.
[83] M.M. Hossain, H.I. de Lasa, AIChE J. 53 (2007) 1817–1829.
[84] M.M. Hossain, D. Lopez, J. Herrera, H.I. de Lasa, Catal. Today 143 (2009) 179–186.
[85] K. Sohlberg, S.J. Pennycook, S.T. Pantelides, Chem. Eng. Commun. 181 (2000) 107–135.
[86] D. Coster, a. L. Blumenfeld, J.J. Fripiat, J. Phys. Chem. 98 (1994) 6201–6211.
[87] X. Liu, J. Phys. Chem. 2 (2008) 5066–5073.
[88] C. Choong, L. Huanga, Z. Zhonga, J. Lina, L. Hong, L. Chen, Appl. Catal. A Gen. 407 (2011) 155–162.
[89] V. Guggilla, J. Akyurtlu, A. Akyurtlu, I. Blankson, Ind. Eng. Chem. Res. 49 (2010) 8164–8173.
[90] W. Gac, Appl. Surf. Sci. 257 (2011) 2875–2880.
[91] G. Xu, K. Shi, Y. Gao, H. Xu, Y. Wei, J. Mol. Catal. A Chem. 147 (1999) 47–54.
[92] H. Liu, D. He, Int. J. Hydrogen Energy 36 (2011) 14447–14454.